UC Riverside

Title

Improved methane emission estimates using AVIRIS-NG and an Airborne Doppler Wind Lidar

Permalink

https://escholarship.org/uc/item/8f3085g5

Authors

Thorpe, Andrew K
O'Handley, Christopher
Emmitt, George D
et al.

Publication Date

2021-12-01

DOI

10.1016/j.rse.2021.112681

Peer reviewed

Improved methane emission estimates using AVIRIS-NG and an Airborne Doppler Wind Lidar

Andrew K. Thorpe [a,*], Christopher O'Handley [b], George D. Emmitt [b], Philip L. DeCola [c], Francesca M. Hopkins [d], Vineet Yadav [a], Abhinav Guha [e], Sally Newman [e], Jorn D. Herner [f], Matthias Falk [f], Riley M. Duren [a,g,h]

[a] *Jet Propulsion Laboratory, California Institute of Technology, USA*
[b] *Simpson Weather Associates, Inc., USA*
[c] *University of Maryland, USA*
[d] *University of California Riverside, USA*
[e] *Bay Area Air Quality Management District, USA*
[f] *California Air Resources Board, USA*
[g] *University of Arizona, USA*
[h] *Carbon Mapper*

ARTICLE INFO

ABSTRACT

Estimating methane (CH_4) emission rates using quantitative CH_4 retrievals from the Next Generation Airborne Visible/Infrared Imaging Spectrometer (AVIRIS-NG) requires the use of wind speeds. Model wind speeds have limited temporal and spatial resolution, meteorological station wind data are of variable quality and are often not available near observed plumes, and the use of ultrasonic anemometers co-located with methane sources is impractical for AVIRIS-NG flight campaigns with daily coverage of thousands of square kilometers. Given these limitations, this study focused on the use of the Twin Otter Doppler Wind Lidar (TODWL) to measure near surface winds and provide coincident measurements to CH_4 plumes observed with AVIRIS-NG. In a controlled release experiment, TODWL observed wind speed and direction agreed well with ultrasonic anemometer measurements and CH_4 emission rates derived from TODWL observations were more accurate than those using the ultrasonic anemometer or model winds during periods of stable winds. During periods exhibiting rapid shifts in wind speed and direction, estimating emission rates proved more challenging irrespective of the use of model, ultrasonic anemometer, or TODWL wind data. Overall, TODWL was able to provide reasonably accurate wind measurements and emission rate estimates despite the variable wind conditions and excessive flight level turbulence which impacted near surface measurement density. TODWL observed winds were also used to constrain CH_4 emissions at a refinery, landfill, wastewater facility, and dairy digester. At these sites, TODWL wind measurements agreed well with wind observations from nearby meteorological stations, and when combined with quantitative CH_4 plume imagery, yielded emission rate estimates that were similar to those obtained using model winds. This study demonstrates the utility of combining TODWL and AVIRIS-NG CH_4 measurements and emphasizes the potential benefits of integrating both instruments on a single aircraft for future deployments.

1. Introduction

Over the last three decades, the growth rate of atmospheric methane (CH_4) has varied, slowing between 1999 and 2006 then increasing with an acceleration since 2014 (Nisbet et al., 2019). Methane is a long-lived greenhouse gas with a global warming potential 86 times that of carbon

dioxide on a 20-year timeframe and contributes approximately 17% of the total radiative forcing attributed to anthropogenic greenhouse gases and halocarbons (Myhre et al., 2013). Therefore, small reductions in CH_4 emissions will result in large reductions in overall atmospheric radiative forcing.

There remains significant uncertainty in the magnitude and

distribution of anthropogenic CH_4 emissions given sources that span multiple sectors and reflect a mixture of biological processes as well as venting and leaks from energy sector infrastructure (Kirschke et al., 2013; Schwietzke et al., 2016; Schaefer et al., 2016). Several recent studies indicate that a small number of strong sources are responsible for the majority of observed CH_4 emissions across multiple emission sectors (Zavala-Araiza et al., 2015; Lyon et al., 2015; Brandt et al., 2014, 2016; Frankenberg et al., 2016; Duren et al., 2019; Cusworth et al., 2021). Identifying strong emission sources offers the potential to constrain regional greenhouse gas budgets, improve partitioning between anthropogenic and natural emission sources, and to mitigate emissions (Hopkins et al., 2016).

The California Methane Survey was the first systematic state survey to locate CH_4 point sources and quantify emissions using the Next Generation Airborne Visible/Infrared Imaging Spectrometer (AVIRIS-NG) (Duren et al., 2019). Between 2016 and 2017, flights covered approximately 59,000 km^2 and permitted high resolution mapping and emission quantification from 564 strong point sources spanning the energy, waste management, and agriculture sectors. For the California Methane Survey, AVIRIS-NG typically flew at 3 km above ground level, resulting in a detection threshold around 10 kg hr^{-1} (Duren et al., 2019). CH_4 emissions were estimated as the product of the integrated mass enhancement in plumes observed by AVIRIS-NG and 10 m modelled winds from 3 km resolution reanalysis data (NOAA's High-Resolution Rapid Refresh HRRRv3). However, uncertainty from this wind product introduces considerable error into the emissions calculation given the coarse spatial and temporal resolution of 1 h averaged 10 m winds from HRRR.

Previous studies have indicated that considerable uncertainties in wind speed propagate into emission rate estimates using imaging spectrometers. For example, Varon et al. (2018) estimate these uncertainties range from 5 to 50% for simulated results and from 30 to 90% from observed results using the GHGSat instrument and winds from a sample of the GEOS-FP global database. For the AVIRIS-NG Four Corners campaign, Frankenberg et al. (2016) assumed one average wind speed (2 m s^{-1}) to conservatively estimate emission rates with estimated errors driven solely by wind speed uncertainty. Duren et al. (2019) reported emission rate uncertainty that ranged from ±4 to ±95% (mean 30%) after discarding about 20 flux estimates with uncertainty >100% using modelled winds (HRRRv3) together with CH_4 plumes observed with AVIRIS-NG.

The use of HRRR winds has significant limitations given the grid cell of only 3 km, the 1 h timestep, and the associated wind speed uncertainties utilize calculations that span the 9 nearest grid cells (total area of 81 km^2) and three time-steps (plume detection time ± 1 h). Existing meteorological station wind data can be used but datasets are of variable quality and are often not available near observed plumes. While field deployed ultrasonic anemometers (referred to as anemometer below) can provide accurate near-surface winds, their use is impractical for AVIRIS-NG flight campaigns with daily coverage of thousands of square kilometers.

Given these limitations, this study focused on the use of the Naval Postgraduate School's Twin Otter Doppler Wind Lidar (TODWL) to measure near-surface winds, cover large regions rapidly, and provide coincident measurements to CH_4 plume observations by AVIRIS-NG. As an initial proof of concept, AVIRIS-NG and TODWL were operated on separate aircraft platforms, however, an ideal future deployment would integrate both instruments on the same platform (see Section 6). Previous controlled release experiments using only AVIRIS-NG focused solely on determining CH_4 detection thresholds rather than estimating emissions (Thorpe et al., 2016). In this study, CH_4 emissions from a controlled release experiment were estimated using winds derived from TODWL and compared with results obtained using an in situ anemometer and HRRR. Further, remotely sensed TODWL wind speed and direction measurements were compared to those obtained from several anemometers located near the Twin Otter flight path. Additional results

are presented for a refinery, landfill, wastewater treatment facility, and dairy.

2. Methane plume mapping with AVIRIS-NG

2.1. AVIRIS-NG instrument

AVIRIS-NG measures solar backscatter in the 380 to 2500 nm range at approximately 5 nm spectral resolution and sampling (Hamlin et al., 2011). With a 34° field of view, this push broom instrument (Fig. 1a) covers large regions quickly with an image spatial resolution that scales with flight altitude, typically ranging from 3 to 8 m for 3–8 km flight level above ground. AVIRIS-NG was first used for CH_4 mapping with a controlled release experiment that demonstrated consistent detection of emissions as low as 10 kg CH_4 h^{-1} across multiple flight altitudes and wind conditions (Thorpe et al., 2016).

Since 2015, there have been a number of AVIRIS-NG campaigns aimed at characterizing point source CH_4 emissions in Colorado, New Mexico, California, Alaska, Canada, and Texas. A study in the Four Corners region characterized over 250 individual CH_4 plumes associated with coal bed CH_4 extraction, with the top 10% of emitters responsible for half of the total observed point source contribution (Frankenberg et al., 2016). The California Methane Survey identified and quantified point source emissions from multiple emission sectors with 0.2% of the surveyed infrastructure contributing 34–46% of California total CH_4 inventory (Duren et al., 2019). A flight campaign in the Permian Basin identified 1100 CH_4 sources, with 50% of detected emissions resulting from oil and gas production, 38% from gathering and boosting, and 12% from processing (Cusworth et al., 2021). Additional studies have explored the underground gas storage (Thorpe et al., 2020) and waste management sectors (Krautwurst et al., 2017; Cusworth et al., 2020), sources in the San Francisco Bay area (Guha et al., 2020), and CH_4 hotspots associated with thermokarst lakes (Elder et al., 2020).

AVIRIS-NG CH_4 retrievals are based on absorption spectroscopy in the shortwave infrared between 2100 and 2500 nm (Thorpe et al., 2014, 2016, 2017; Thompson et al., 2015; Cusworth et al., 2019; Foote et al., 2020). In this study, we use a linearized matched filter to first calculate a mixing ratio length in units of parts per million per meter (Thompson et al., 2015) for AVIRIS-NG flights flown at 3 km above ground, providing an image swath of 1.8 km with 3 m image pixels.

2.2. Quantifying CH_4 emissions

Emission rates are estimated by combining the integrated mass enhancement (IME), plume length and wind speed, which has been demonstrated in previous studies (Frankenberg et al., 2016; Duren et al., 2019; Thorpe et al., 2020; Cusworth et al., 2020; Cusworth et al., 2021). To isolate each AVIRIS-NG plume, we select image pixels for inclusion using a mixing ratio threshold of 500 ppmm (parts per million per
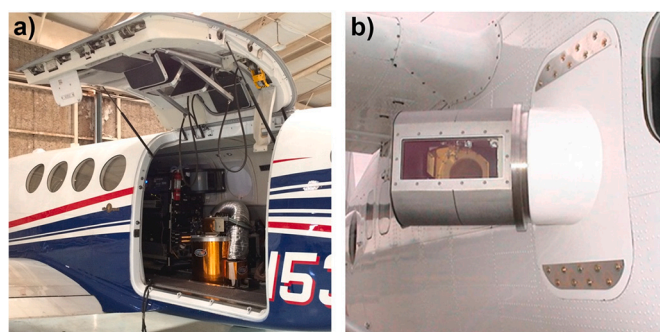

Fig. 1. Instruments used in this study. a) AVIRIS-NG imaging spectrometer installed in King-Air aircraft. b) TODWL with its scanner mounted in a starboard door of the Naval Post Graduate School's Twin Otter.

meter), a maximum fetch radius of 150 m from the plume origin, and a merge distance of 20 m (effectively a 20 m sliding window that determines which components of the plume are used in the IME calculation), consistent with previous studies (Duren et al., 2019; Thorpe et al., 2020). Centered on the plume origin, an initial circle of radius (r_1) was defined based on the pixel size (3 m). For the plume area covered by this circle, the excess mass of CH_4 in the plume (IME) was calculated as follows:

$$IME_{r_c} = k \sum_{i=0}^{n} \alpha(i)S(i) \tag{1}$$

as the summation of the CH_4 mixing ratio length (α) that represents a CH_4 enhancement in parts per million per meter (ppmm) for the n pixels in the plume over the pixel area S, which is converted to CH_4 mass units with the constant k (Frankenberg et al., 2016; Thompson et al., 2015). Next, the radius (r_c) was sequentially expanded for the total number of circles c, and a new IME for the given radius (IME_{r_c}) was calculated. For the entire range of radii (r_c), starting at the plume origin then sequentially expanding until the full extent of the plume is reached, the IME was divided by the radius (IME_{r_c}/r_c) and the average ($\overline{IME}/r$) and standard deviation were calculated to represent uncertainty (σ_{IME}) in the estimates. Additional details on the calculations and figures showing an example of the concentric circles are provided in Duren et al. (2019, Fig. S.3) and Thorpe et al. (2020, Fig. S3).

The CH_4 emission rate for a given plume (Q, in kg CH_4 hr^{-1}) was calculated:

$$Q = \left(\overline{IME}/r \right) U_{10} \tag{2}$$

where $\overline{IME}/r$ is the average ratio for the range of radii and U_{10} is the average wind speed at 10 m above ground level.

Finally, a total uncertainty (σ_Q), reflecting the combined uncertainties associated with the IME/r calculation and wind measurements was calculated as follows:

$$\sigma_Q = Q \left(\left(\frac{\sigma_{\overline{IME}/r}}{\overline{IME}/r} \right)^2 + \left(\frac{\sigma_U}{U_{10}} \right)^2 \right)^{\frac{1}{2}} \tag{3}$$

This uncertainty estimate assumes the variability (standard deviation) in each term is independent and uncorrelated. In previous studies (Duren et al., 2019; Thorpe et al., 2020; Cusworth et al., 2021), 10 m wind speeds were obtained from NOAA's High-Resolution Rapid Refresh (HRRRv3) 3 km product (Benjamin et al., 2016). Average (U_{10}) and standard deviation (σ_U) values were calculated using 27 HRRR grid cells, including a 3 × 3 box centered on the source and repeated for 3 timesteps (plume detection time ± 1 h), which reflects a spatial and temporal estimate of variance. Additional details on the HRRR data and variable fields can be found in Appendix A. For this study, emissions were estimated using winds derived from HRRR, TODWL, and an in situ anemometer. A description of the average and standard deviation calculation for each type of wind measurement is provided above for HRRR, in Section 3.2 for TODWL, and in Section 5.1.2. for the in situ anemometer.

3. Measuring near-surface winds with airborne Doppler wind lidar

In 1999, the Office of Naval Research funded the development of an Airborne Doppler Wind Lidar (ADWL) to be flown on the Naval Postgraduate School's Twin Otter (Fig. 1b) and referred to as the TODWL. The TODWL is one of just a few ADWLs available for atmospheric research in the United States (Emmitt et al., 2005b; Emmitt, 2007).

While this ADWL was initially developed for marine atmospheric boundary layer research in support of a space-based Doppler wind lidar design project, it has since been used for numerous science investigations of organized large eddies and mass fluxes in the atmospheric boundary layer (Emmitt and O'Handley, 2003; Emmitt et al., 2005a, 2005b; Emmitt et al., 2015a; Emmitt, 2019), complex flows in mountainous topography (Greco and Emmitt, 2005; Emmitt et al., 2014a; Pal et al., 2016; De Wekker et al., 2012), as well as practical studies such as wing tip vortices (Emmitt et al., 2014b; Emmitt and O'Handley, 2015), precision airdrops (Emmitt and Greco, 2013; Emmitt et al., 2015b) and drone energy harvesting (Emmitt et al., 2017). The Twin Otter is an ideal aircraft for lower tropospheric and near surface research and usually flies at slow cruise speeds (~50 m s^{-1}) and low altitudes (~10 m) over the ocean and other bodies of water. This capability has enabled both remote sensing and in situ sensing of boundary layer processes.

3.1. TODWL instrument and its precision wind measurements

The TODWL measures the range gated Doppler shift of the backscattered return pulse along the laser beam caused by the motion of aerosols. The TODWL operates at an eye safe wavelength of 2.0 μm with a low pulse energy of 2.0 mJ at a pulse rate of 500 Hz. It can take measurements as close as 0.4 km and as far away as 25 km depending upon the amount and distribution of aerosol backscatter. TODWL uses a bi-axial scanning cylinder mounted on the right side of the plane (Fig. 1b). This allows a wide range of viewing angles (±120° in elevation and 0–60° in azimuth) with the primary restriction being near horizontal views to the left and right. The scanner rotates at 30° s^{-1} between stare locations and the scanning pattern is fully programmable during flight. For this study, the scanner was programmed to stare for 1 s at each of 9 prescribed angles between 0 and 40° azimuth; each scan took 15 s to complete. Additional details concerning the TODWL instrument and data processing can be found in Godwin et al. (2012).

Full vector wind profiles are retrieved from line of sight velocity (VLOS) measurements having multiple perspectives within a volume. Generally, TODWL uses a conical step-and-stare scan pattern around the vertical axis with a 20–30° off nadir angle to obtain wind profiles. The lidar beam is pointed in 12 different directions, thus obtaining a set of VLOS distributed by height (ranges gates) and angular perspective. A least square fit to the VLOS at each range gate is then used to obtain wind vectors at each height level. However, one limitation of the TODWL receiver is saturation that occurs when a return from the ground or thick cloud is encountered. In practice, for a 20° off nadir scan, this makes it impossible to obtain winds below about 150 m above ground level (AGL) (Godwin et al., 2012). To circumvent this problem, a unique forward scanning and data processing strategy was developed to allow winds to be obtained as low as 15–30 m AGL (Section 3.2).

The precision of radial wind measurements obtained with TODWL during ideal non-turbulent flight is on the order of 0.2 m s^{-1} with a bias of <0.1 m s^{-1} (De Wekker et al., 2012). The precision is determined primarily by the digitization rate of the returning signal and the frequency resolution of the Fast Fourier Transform. In most TODWL applications, 25 individual shots (~150 milliseconds, equivalent to ~10 m of aircraft forward motion) are accumulated to provide enhanced sensitivity to the aerosol backscattered returns as well as to average out any jitter due to beam pointing and laser outgoing frequency. These measurement values have been determined over many campaigns using ground returns (zero speed calibration) and comparisons with anemometers, dropsondes, and in situ wind sensors on the Twin Otter.

3.2. Scanning and data processing for CH_4 flights

To obtain winds as close to the ground as practical, a shallow angled (−8°), forward-looking scan was developed that uses 9 stare points from 0 to 40° azimuth (every 5°) to the right of the flight track. During the

CH_4 flights, the Twin Otter was typically flying with about $+4°$ of pitch up; the $-8°$ scan angle yields an effective laser beam line of sight elevation angle relative to earth of $-4°$. This geometry routinely obtained VLOS measurements at 30–40 m AGL (occasionally to 15 m depending on topography and turbulence) and required a relatively low aircraft flight level about 500 m AGL. ADWLs using the latest technology would not require such a low flight level to achieve wind measurements within the lowest 30 m of the boundary layer (see Section 6).

Significant turbulence was encountered within the strongly convective atmospheric boundary layer during the controlled release flights. Fig. 2a shows selected Twin Otter attitude parameters for two flights. One is at higher altitude (1300 m AGL; red curve) and represents more typical flight conditions marked by slow, low amplitude variations. The second, from one of the controlled release flights at 500 m AGL (blue curve), reveals strong flight level turbulence. During many of the controlled release flight passes it was not uncommon for pitch and roll to vary by 3–4° and at times up to 8° during a single scan. This turbulence significantly scattered individual lines of sight within the general target volume centered on the CH_4 source. Fig. 2b shows an ideal TODWL 9 point scan (red dots marking locations where the lidar beam intersects ground) versus an actual scan impacted by turbulence (connected black dots). In calm conditions, a roughly linear set of observations perpendicular to the flight track would be acquired, nearly centered on the target and approximately 2.5 km in length. However, the actual ground intersection points are widely scattered with many terminating in higher ground SW of the target when the aircraft pitched down. At other times the aircraft pitched up and individual lines of sight passed well above the target. As a result, individual 9-point scans rarely yielded enough data points near the target to produce acceptable wind vectors.

To compensate for the reduced and variable measurement density caused by turbulence, a binning scheme was developed to aggregate VLOS measurements from multiple scans during each flight pass. First, a set of 3-dimensional boxes on a 0.01° horizontal grid (and every 10 m in the vertical) was centered at and around the target. Then, all the VLOS measurements that fell within each box were combined, regardless of timing. These VLOS measurements were used to compute a wind vector which was assigned to the center of the box. Thus, instead of relying on only 9 (usually fewer) VLOS values from a single scan, data from any scan was used in the fitting procedure provided it fell within the target box, the total azimuth range was at least 20°, and there were at least 10 measurements available. One consequence of this approach is that the effective averaging period varies depending on conditions during each flight pass. For instance, during the controlled release flights the mean time window was 79 s but ranged from 11 to 148 s.

The best results were obtained using 0.04° boxes that were 20 m deep, effectively averaging lidar measurements over ~16 km^2. This provided enough input measurements (VLOS) to yield good fits while limiting redundancy/overlap with neighboring grid points. Fig. 2c shows an example of the data distribution for one flight pass during the controlled release experiment. All the VLOS measurements within the 20–40 m AGL layer from a single flight pass are plotted together with the box centered on the controlled release site. It is evident how the data distribution varies due to aircraft motions; in this example, most of the available data points in the box are located east of the target site.

Generally, the lowest level at which TODWL winds were available was 30 m AGL. Since CH_4 emission calculations use 10 m winds, the TODWL wind speeds were adjusted to 10 m using a standard power law relationship:

$$V_{10} = V_z(10/z)^K \qquad (4)$$

where V_{10} is velocity (m s^{-1}) at 10 m AGL, V_z is TODWL wind velocity at observation level z, z is height of TODWL observation in meters AGL, and K is an exponent dependent upon atmospheric stability. The value of K was determined after data collection but prior to data processing. $K = 0.143$ is a standard value that is used for neutral stability conditions. However, Newman and Kein (2014) found that for strongly heated late summer conditions in the U.S. Central Plains, $K = 0.1$ was more appropriate. The conditions during the controlled release and the dairy flights fit this strongly heated environment so we used $K = 0.1$ for these, and the more standard $K = 0.143$ for the Bay area cases which were more influenced by the marine layer. Use of 0.1 and 0.143 for K results in a 10.4% and 14.5% reduction of wind speed from 30 to 10 m.

The final TODWL product was a 3-dimensional vector wind field for each flight pass along with an estimated 10 m wind speed/direction and standard deviation at each target site. The standard deviation estimates were computed using the wind vectors at the target site and the 8 surrounding grid points, reflecting an area based estimate of variance over 36 km^2. Evaluation of residual ground velocities (ideal value = 0 m s^{-1})
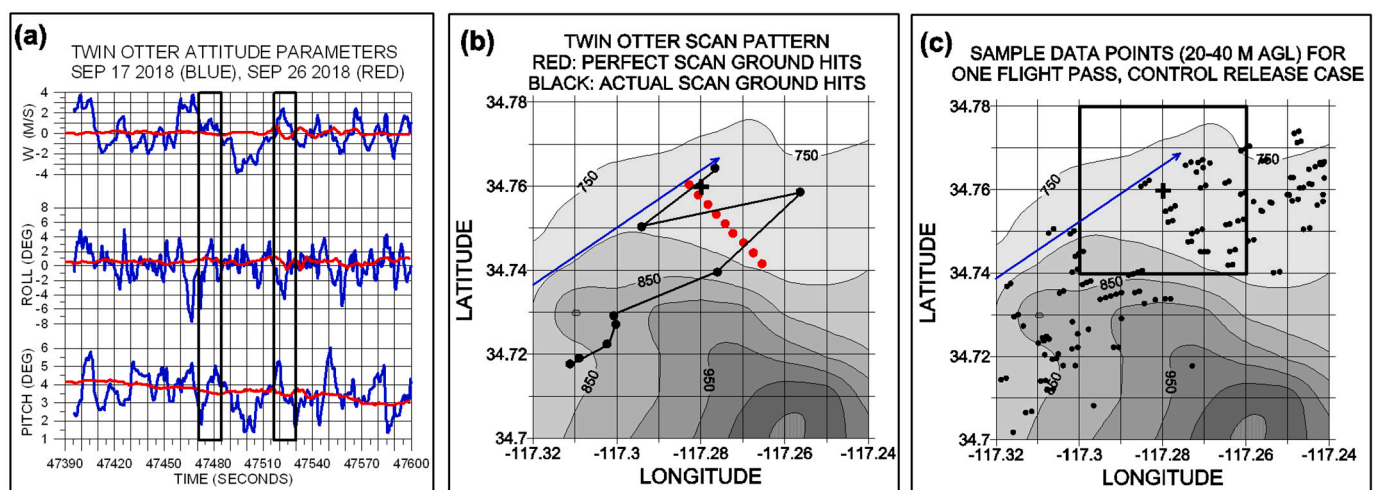

Fig. 2. Atmospheric turbulence and its impact on TODWL near-surface sample distribution. a) Twin Otter vertical velocity (w), roll and pitch for a normal low-turbulence flight at 1300 m AGL (red) and a highly turbulent controlled release flight at 500 m AGL (blue). Black vertical bands mark boundaries of 2 representative 9-point lidar scans. b) TODWL scan pattern. Red dots indicate ground intersection points for an ideal scan while connected black dots show one actual scan from the controlled release case. c) Distribution of all near surface measurements during one controlled release pass. Black dots show all data points within 20–40 m AGL from multiple scans. For clarity, black dots representing individual scans are not connected. On panels b and c, the blue line is Twin Otter flight track, the plus sign is the controlled release site. Square on panel c is the 0.04° box centered on the controlled release site. Topography resolution is 50 m (grey shading). (For interpretation of the references to colour in this figure legend, the reader is referred to the web version of this article.)

revealed a $+0.2\,\mathrm{m\,s^{-1}}$ bias with a standard deviation of $0.3\,\mathrm{m\,s^{-1}}$ during the controlled release flights. This indicates that aircraft motions and turbulence were adequately accounted for during processing. Despite the turbulence and relatively large averaging region, TODWL winds were consistent with near surface winds measured by an anemometer during the controlled release experiment (Section 5.1) as well as with surface meteorological stations near the other sites (Section 5.2).

Individual flight passes were timed so that AVIRIS-NG and TODWL were viewing the plumes at essentially the same time. However, the impact of minor differences in flight timing as well as turbulence meant that measurements were not precisely contemporaneous. In order to match AVIRIS-NG and TODWL results, UTC times were extracted for each AVIRIS-NG plume and TODWL observation for each set of flight passes. The TODWL 10 m wind speed/direction was reported with a UTC time that reflects the average time of the individual VLOS measurements that were used. For the controlled release experiment, the difference between AVIRIS-NG and TODWL measurements averaged 49.4 s (minimum 4.9 and maximum 125.2 s).

4. Study sites

Coordinated AVIRIS-NG and TODWL flights were performed on 17 Sept. 2018 for a controlled CH_4 release experiment near Victorville, California, on 19 Sept. 2018 for dairies in the San Joaquin Valley, as well as on 20 and 27 Sept. 2018 for a mixture of landfills, refineries, and wastewater treatment facilities in the San Francisco Bay area.

AVIRIS-NG was flown in a King Air B-200 at a flight altitude of 3 km AGL, resulting in images with a 1.8 km swath width and 3 m pixel size. For each target, AVIRIS-NG flew an identical flight line multiple times. TODWL measurements were acquired using a Twin Otter aircraft at a flight altitude of 500 m AGL. For the controlled release experiment the Twin Otter aircraft flew the same heading as the King Air but the flight line was offset to the port side by several hundred meters given the TODWL viewing geometry. For the remaining targets, the Twin Otter aircraft flew different headings than the King Air, but performed multiple overpasses using the same flight path.

The controlled CH_4 release experiment was performed at a Pacific Gas and Electric Company (PG&E) natural gas pipeline junction located approximately at $34.75°$, $-117.27°$ at 763 m MSL (Fig. 3c). PG&E staff used MERIGAUGE Model 3900 pressure gauges and an American Meter Series 1800 Worker/Monitor Regulator to control gas pressure as well as a GE Roots Meter 5M175 to measure the emission rate. During the
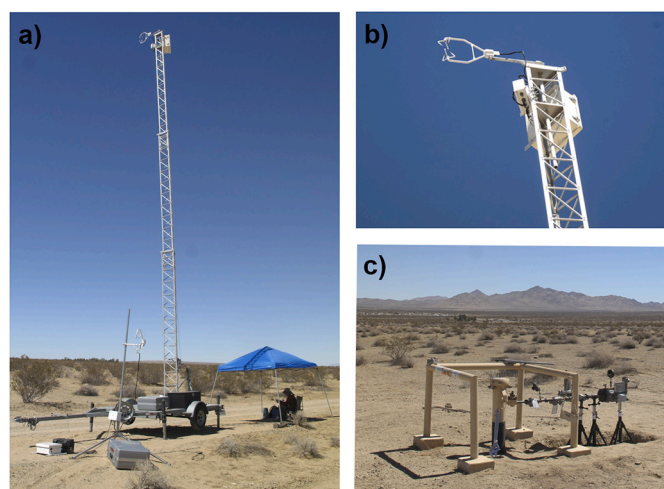

Fig. 3. CH_4 controlled release experiment setup. a) 10 m tower. b) Ultrasonic anemometer. c) Pressure gauges, a regulator, and a flow meter were attached to a natural gas pipeline which permitted controlled CH_4 releases at 0.75 m above ground.

controlled release experiment, the release point was 0.75 m above ground and the emission rate was adjusted by changing the set point pressure on the regulator. The emission rate was measured using the meter, which has a reported accuracy of $\pm 2\%$. Natural gas that was 94.89% CH_4 as measured by PG&E resulted in a metered release rate that began at 47.5 kg $CH_4\,\mathrm{hr^{-1}}$ (19:00–20:15 UTC) and was increased to 101.7 kg $CH_4\,\mathrm{hr^{-1}}$ (20:15–21:30 UTC).

A 10 m tower was positioned 26 m from the CH_4 release point and equipped with an ultrasonic anemometer (CSAT3, Campbell Scientific) that provided 10 Hz wind measurements at 10 m above ground level (Fig. 3a, b). During this period, conditions were marked by clear skies and strong heating, with temperatures ranging between 32.2 and 35.0 °C with highly variable wind conditions with speeds between 0 and 8 $\mathrm{m\,s^{-1}}$ and spanning all directions (see Fig. 5).

Based on previous CH_4 observations from California Methane Survey flights, a number of CH_4 producing facilities were also flown with AVIRIS-NG and TODWL. Here we summarize examples from a San Francisco Bay Area refinery, landfill, wastewater facility, and a dairy digester near Corcoran, CA. For the refinery, ground based meteorological measurements ($37.953830°$, $-122.379700°$, 2 m elevation) were provided by the Bay Area Air Quality Management District (BAAQMD). Publicly available weather station wind data were also used for comparison with TODWL results at the refinery, landfill, wastewater facility, and dairy digester.

5. Results

5.1. Controlled methane release

5.1.1. Methane plume imagery

Plumes of CH_4 from the natural gas release were clearly visible at both the 47.5 and 101.7 kg $CH_4\,\mathrm{hr^{-1}}$ emission rates, and plume shapes agreed well with wind direction and wind speeds. Fig. 4 shows CH_4 plumes overlaid on AVIRIS-NG true colour imagery with the controlled release location in the center of the image. Typically, higher CH_4 enhancements are visible at or near the controlled release location with decreasing concentrations downwind. The grey lines indicate the estimated wind direction derived from plume shape by fitting a line to the CH_4 pixels within each plume. For example, Fig. 4a shows a well-defined plume for the 47.5 kg $CH_4\,\mathrm{hr^{-1}}$ emission rate for winds from the northwest and a 2.4 $\mathrm{m\,s^{-1}}$ wind speed as measured with the anemometer. For the example shown in Fig. 4b for 101.7 kg $CH_4\,\mathrm{hr^{-1}}$, the wind speed drops to 0.5 $\mathrm{m\,s^{-1}}$ resulting in the compact appearance of the plume. Fig. 4c shows winds from the south (2.9 $\mathrm{m\,s^{-1}}$) and evidence of turbulent mixing in the form of eddies downwind of the CH_4 release for this 101.7 kg $CH_4\,\mathrm{hr^{-1}}$ example. In contrast, Fig. 4d shows a more elongated plume consistent with the increased wind speed (3.9 $\mathrm{m\,s^{-1}}$) for the same emission rate.

5.1.2. Wind measurements

Fig. 5 shows high resolution (10 Hz) wind speed and direction as measured by the anemometer (grey), with blue circles and error bars representing the mean and standard deviation of the 79 s interval centered on each TODWL observation. Similar values are provided for TODWL (red); wind direction is from the 30 m observation while the plotted wind speed is reduced to 10 m using Eq. (4) with $K = 0.1$. It is important to note that TODWL is essentially reporting an average value over a 4×4 km box (see Section 3.2), which is a much larger spatial footprint than the point measurement of the anemometer. Therefore, while the two should track similarly with time, deviations are to be expected from pass to pass, especially during times of increased wind variability. Finally, HRRR wind speeds are shown in green in Fig. 5a while wind directions estimated from AVIRIS-NG plumes are shown in Fig. 5b (green). Because HRRR winds are available only at 1-h timesteps, the average and standard deviation are often identical for successive plume observations (see Section 2.2). The error bars shown in Fig. 5
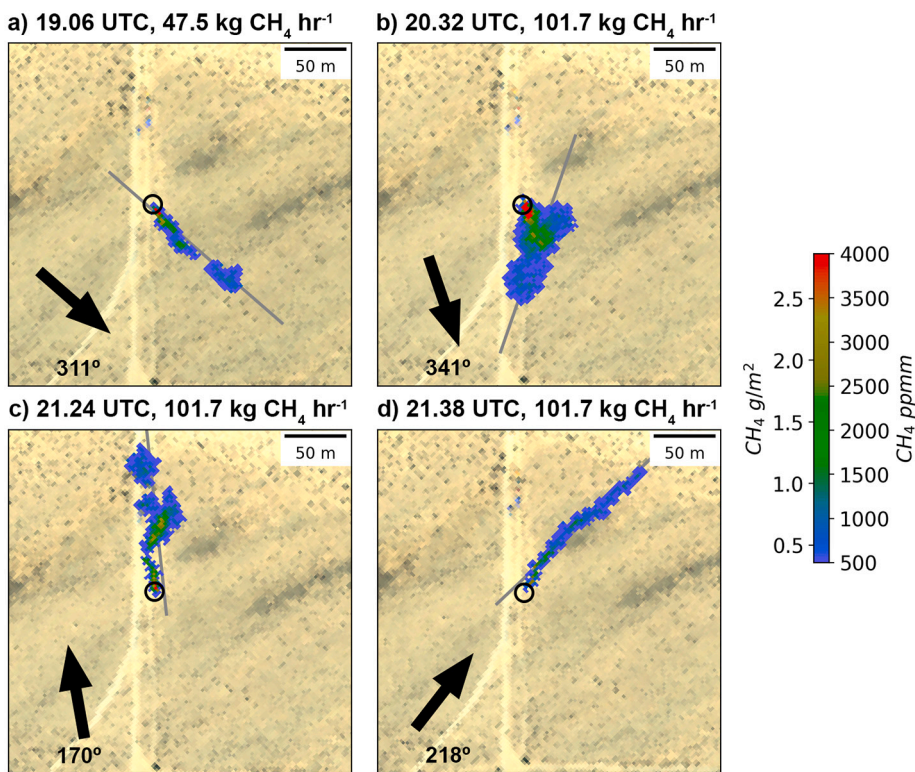
Fig. 4. AVIRIS-NG CH₄ plumes for the controlled release experiment overlaid on true colour imagery with shapes influenced by emission rate as well as wind speed and direction. Grey lines indicate estimated wind direction derived from plume shape as compared with wind direction measured by the anemometer (black arrows). The center of the black circles indicates the location of the release. a) For the plume observed at 19.06 UTC, anemometer wind speed was 2.4 ± 0.5 m s⁻¹. b) 20.32 UTC, 0.5 ± 0.3 m s⁻¹. c) 21.24 UTC, 2.9 ± 0.5 m s⁻¹. d) 21.38 UTC 3.9 ± 0.7 m s⁻¹. Colour bar shows the observed CH₄ enhancement in units of ppmm and g m⁻².
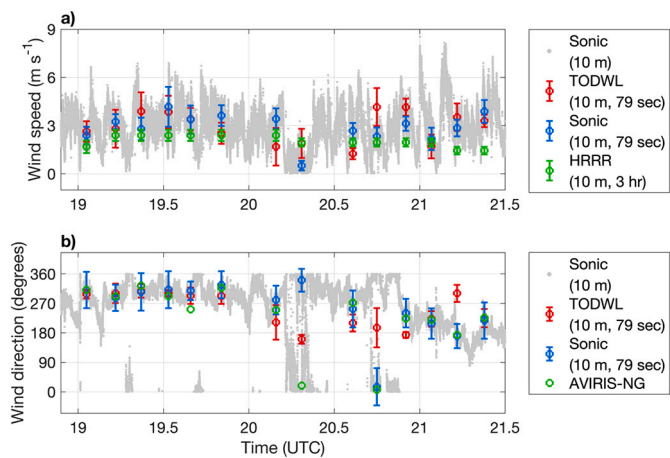

Fig. 5. a) Comparison of wind speed as measured by ultrasonic anemometer (sonic), TODWL, and HRRR model data during a controlled release experiment. Grey trace shows raw 10 Hz ultrasonic anemometer data, and coloured points with associated error bars represent mean and standard deviation of each time-averaged dataset. Although HRRR winds are hourly, the average HRRR wind speeds are shown for each of the plume observations to permit direct comparison between wind speeds. b) Wind direction measured by ultrasonic anemometer (sonic), TODWL, and inferred from AVIRIS-NG CH₄ plume imagery (see Section 5.1.1). Error bars represent measurement uncertainty based on different measurement approaches (see Section 2.2 for HRRR, Section 3.2 for TODWL, and in Section 5.1.2. for ultrasonic anemometer).

represent measurement uncertainty based on different measurement approaches (see Section 2.2 for HRRR, Section 3.2 for TODWL, and in Section 5.1.2. for anemometer). Over this period, results from all flights are shown except at 20.0 UTC due to an AVIRIS-NG instrument artifact and at 20.5 UTC due to insufficient data coverage (18° azimuth range) for TODWL.

Prior to 20.0 UTC (Fig. 5) there was good agreement among all

measurements, though HRRR wind speed tended to be low. The wind was generally from the WNW (~300°) with mean speeds of 2.5–4.0 m s⁻¹ and occasional gusts to 6–7 m s⁻¹. After 20.0 UTC, a period of enhanced variability developed and larger differences were noted among all measurements. This was especially pronounced between 20.0 and 20.5 UTC when winds became light and variable. For instance, at 20.2 UTC the TODWL wind was 212° at 1.7 m s⁻¹ while the anemometer yielded 280° at 3.4 m s⁻¹. During the following pass (20.3 UTC), the TODWL wind was 160° at 1.9 m s⁻¹ while the anemometer showed the wind becoming nearly calm (341° at 0.5 m s⁻¹), consistent with the compact appearance of the plume at this time (Fig. 4b).

Another period of enhanced wind variability occurred around 20.8 UTC when the largest wind speed and direction difference was observed (TODWL 196°, 4.2 m s⁻¹; sonic 15°, 2.3 m s⁻¹). Thereafter, all datasets showed winds shifting to a more southerly direction though at 21.3 UTC the TODWL showed a temporary shift back to NW winds. Throughout the period, HRRR winds were nearly constant (1.4–2.4 m s⁻¹) and weaker than observed by both the anemometer and TODWL except during the nearly calm period around 20.3 UTC. Overall, the mean wind speeds from anemometer and TODWL were identical (2.9 m s⁻¹) over the course of the experiment. In contrast, the mean HRRR wind speed during the flight period was considerably less (2.0 m s⁻¹). Some additional figures comparing wind speeds from the 3 sources can be found in Appendix B.

Fig. 6 shows the distribution of TODWL 30 m AGL wind vectors (speeds have been reduced to 10 m) across the analysis domain for selected times. The anemometer and plume wind vectors are also shown near the controlled release point, with an inset image showing the CH₄ plume for each time. For scale, the TODWL analysis box (0.04° square) centered at the controlled release point is shown outlined in black. Recall that all the individual VLOS measurements in that box were used to compute the wind vector at the controlled release site at the center of the box.

As discussed earlier, prior to 20.0 UTC there was broad WNW flow across the region, with generally good agreement between TODWL, anemometer, and AVIRIS-NG plume derived winds. This is
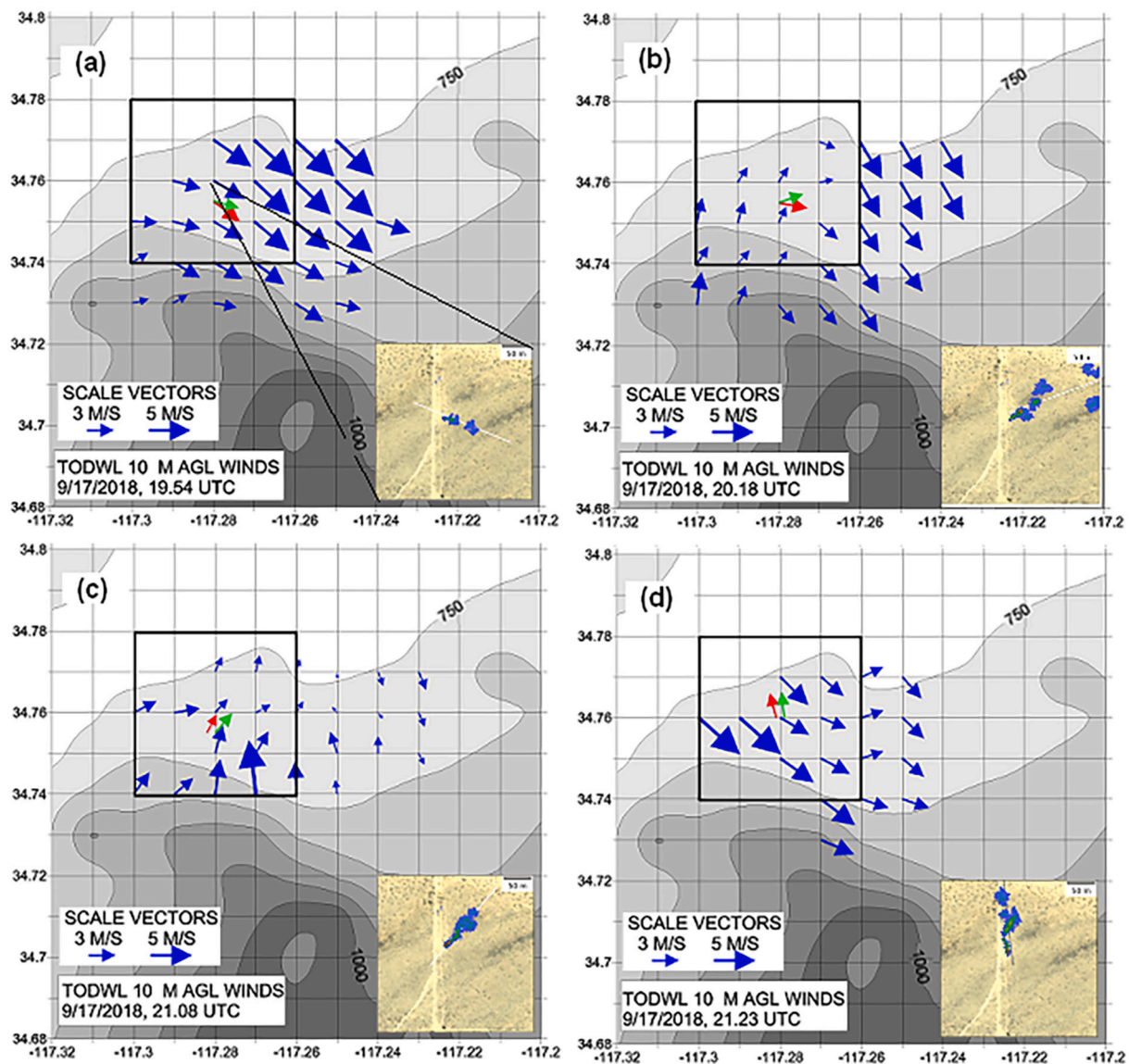
Fig. 6. TODWL wind vectors for 4 times during the controlled release experiment. Arrows represent winds from TODWL (blue), anemometer (red), and wind direction derived from AVIRIS-NG plume (green). Scale vectors apply to TODWL and anemometer winds; AVIRIS-NG vector represents direction only. Black square represents TODWL averaging box centered on the controlled release site. Grey contours indicate terrain heights every 50 m (grey shading). The corresponding image subset that contains the CH_4 plume image from AVIRIS-NG is provided in the lower right of each panel. Image subset is about 285 m in width and is centered on control release site as shown by lines on panel a. (For interpretation of the references to colour in this figure legend, the reader is referred to the web version of this article.)

demonstrated by the TODWL wind vectors at 19.5 UTC (Fig. 6a). The wind directions all agreed within 20° while wind speeds were also similar (3.9 m s^{-1} TODWL, 4.2 m s^{-1} anemometer). Even during this period, TODWL shows fairly significant wind speed variations around the region.

By 20.2 UTC (Fig. 6b) larger differences were noted. The TODWL wind vectors indicated the presence of a wind shift in the vicinity of the release point, with NW (SW) winds to the east (west). The TODWL wind speed (1.7 m s^{-1}) was considerably lower than the anemometer value (3.4 m s^{-1}). In addition, the wind directions from both the anemometer and AVIRIS-NG (280° and 250°) were more westerly than TODWL (212°). These differences are most likely explained by averaging of the varying wind components within the larger TODWL data box. While this averaging may be having a negative impact on the wind estimate compared to the anemometer, TODWL is revealing the presence of complex flow fields that cannot be identified from a single point measurement, but which could impact plume motion and flux estimates and

provide a measure of confidence in individual overpasses.

Around 21.0 UTC (Fig. 6c) winds indicated by anemometer and AVIRIS-NG had shifted to southerly. The TODWL vector field at 21.1 UTC indicates mostly southerly winds in the boxed region, though elsewhere there are lighter winds with variable directions (mainly to the east). All measurements are similar at this time, with wind speeds within 0.5 m s^{-1}. Thereafter, near-surface winds remained southerly as indicated by anemometer and AVIRIS-NG (see Fig. 5b), though TODWL revealed a brief period of stronger WNW winds (3.5 m s^{-1} compared to 2.9 m s^{-1} from anemometer) at 30 m AGL at 21.23 UTC (Fig. 6d).

Fig. 7 shows a time-height section of TODWL horizontal wind vectors over the controlled release site. Through 20.0 UTC, winds were uniformly from the WNW at all levels between 2 and 6 m s^{-1}. Thereafter, winds between 30 and 150 m AGL shifted to southerly and strengthened between 20.5 and 21.0 UTC. Peak TODWL winds (8 m s^{-1} near 80 m AGL) were similar to peak 10 m winds observed by the anemometer around and after 21.0 UTC (Fig. 5a). Note that TODWL 30 m winds
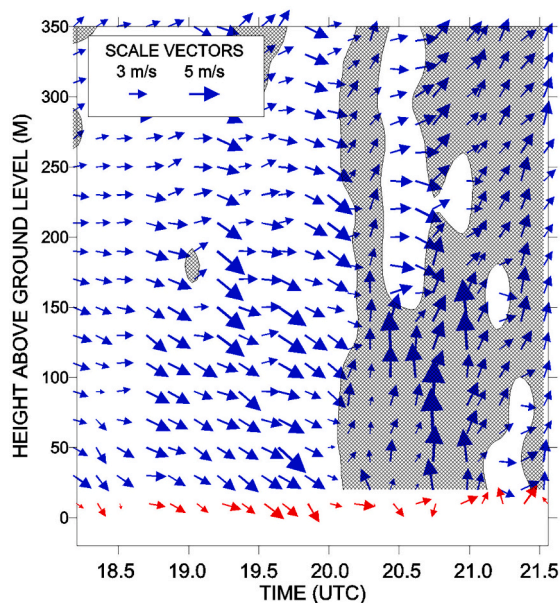
Fig. 7. Time/height cross section of TODWL horizontal wind vectors (blue) directly above controlled release site and anemometer 10 m winds (red). Hatching shows areas with southerly flow component in TODWL data. (For interpretation of the references to colour in this figure legend, the reader is referred to the web version of this article.)

shifted to southerly about an hour before the wind shift was observed by the anemometer at 10 m. This indicates there is a shallow flow near the surface that cannot be seen by TODWL in its scanning configuration and which can explain some of the differences in flux rate estimates at these times (see Section 5.1.3). After 21.0 UTC, TODWL and anemometer winds were more similar with both having southerly components. The exception occurred at 21.2 UTC when the TODWL wind shifted back to WNW (compare with Fig. 6d). This is another example of a limitation of the lidar configuration to fully capture near-surface (< 30 m) winds.

Overall, the time series (Fig. 5), horizontal plots (Fig. 6), and time-height section (Fig. 7) indicate that (1) there was an initial period of deep homogeneous NW flow in the region, (2) a low-level (below 150 m AGL) cyclonic trough or gyre moved into the region from the west, shifting winds to southerly first at 30 m and then at the surface, (3) a brief pulse of NW winds at 30 m in the TODWL data occurs that does not reach the surface. While the detailed nature of these flows is beyond the scope of this investigation, their presence points to the future need to adjust lidar scanning to obtain data closer to the surface.

5.1.3. Flux calculations

Estimated CH$_4$ emissions are shown in Fig. 8a, derived using wind data from HRRR (green), TODWL (red) and the anemometer (blue) for the two controlled release emission rates (horizontal grey lines). During the first 5 passes of the low rate period (19.0–19.6 UTC), there is good agreement between the known emission rate of 47.5 kg CH$_4$ hr^{-1} and the emissions calculated from all wind estimates. This is consistent with the relatively stable wind conditions during this time (Fig. 5), which result in plumes that are closer to steady state conditions, appearing more linear without eddies or plume rotations in downwind portions of the plumes (Figs. 4a, 6a). Both anemometer and TODWL estimates appear to have a small positive bias whereas HRRR estimates are close to the actual release rate. There is some enhanced variability during the final 2 passes, when the anemometer flux estimates were elevated compared to TODWL.

During the high rate period after 20.2 UTC, wind speed and direction were highly variable (0–8 m s^{-1}, 0–360°). This results in plumes that are often appear less linear with eddies and plume rotations (Figs. 4c, 6b, d).
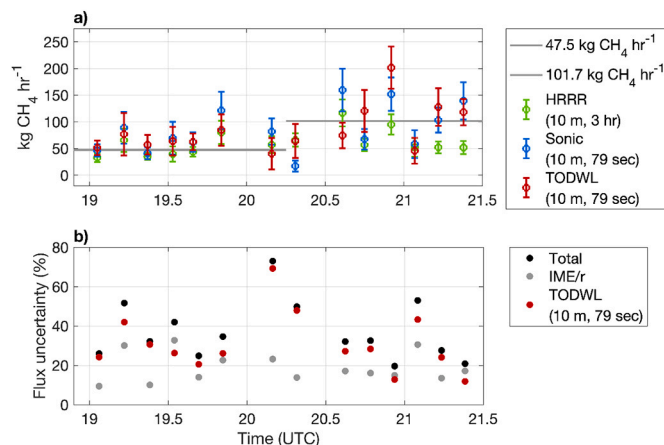

Fig. 8. a) AVIRIS-NG CH$_4$ emission rates derived using TODWL, ultrasonic anemometer (sonic), and HRRR reanalysis wind data. The two known controlled release emission rates are plotted as horizontal grey lines for 47.5 and 101.7 kg CH$_4$ hr^{-1}. Error bars represent measurement uncertainty based on different measurement approaches (see Section 2.2 for HRRR, Section 3.2 for TODWL, and in Section 5.1.2. for ultrasonic anemometer). b) Flux uncertainty budget including uncertainties in the IME/r calculated from the AVIRIS-NG plume imagery and TODWL wind speeds, that are combined as the summation in quadrature (Section 2.2).

Not surprisingly, there is considerably more variation in the estimated emission rates during this period between the measurement systems. At 20.3 UTC, all the emission rate estimates are low. Low wind speed (0.5 ± 0.3 m s^{-1}, anemometer) combined with rapidly shifting wind directions (0–360°) immediately prior (Fig. 5b) could explain the underestimate. Fig. 4b for the 20.3 UTC plume is consistent with these conditions, exhibiting a compact appearance with evidence of rotation immediately prior to the AVIRIS-NG acquisition. Further, the emission rate was adjusted by PG&E staff immediately prior to 20.3 UTC and it is possible that the observed plume more closely reflected the lower emission rate. For the remaining examples there is significantly more variability (Fig. 8a, Table 1) during a period of enhanced wind variability (Figs. 5, 6, and 7). Emission rates calculated using HRRR winds generally underestimate the flux rate especially near the end of the day. Additional plots comparing flux estimates from the 3 sources can be found in Appendix B.

Fig. 8b shows the uncertainty components associated with the emission estimates using the TODWL wind speeds (Section 2.2). Uncertainties associated with the IME/r calculation (grey points) typically range between 10 and 25% with a few outliers up to 33%. As described in Section 2.2, this uncertainty represents variability in the integrated mass enhancement (IME) as calculated by a series of expanding circles centered on the plume origin. The TODWL uncertainties were larger (typically 12–42% with outliers up to 69%). These uncertainties are combined as the summation in quadrature (Section 2.2), resulting in total uncertainties that range between 20 and 48% with a few outliers up to 73%. Referring to Eq. (3) for the 20.2 UTC example, the average TODWL wind speed (U$_{10}$) is low (1.7 m s^{-1}) relative to the 1.2 m s^{-1} standard deviation (σ_U), resulting in a TODWL uncertainty of 70% and the largest emission uncertainty (73%). This is consistent with the presence of a wind shift which introduces uncertainty into the TODWL wind estimate (see Fig. 6b). In contrast, at 20.9 UTC the TODWL wind speed is high (4.2 m s^{-1}) with a 0.5 m s^{-1} standard deviation, which results in a smaller TODWL uncertainty (13%) and total uncertainty (20%).

The large variability in calculated flux rates, especially during the high release rate period, suggests that averaging over multiple flight passes could lead to improved estimates for a given source. Fig. 9a shows average fluxes for the two release rates for the anemometer (blue), the

Table 1

Mean wind speeds, flux rates and standard deviations for the three wind sources for the low and high release rate periods of the controlled release experiment.

Source	Low rate average and standard deviation wind speed (m s^{-1})	Low rate (47.5 kg CH$_4$ hr^{-1})	Low rate uncertainty (%)	High rate average and standard deviation wind speed (m s^{-1})	High rate (101.7 kg CH$_4$ hr^{-1})	High rate uncertainty (%)
TODWL	2.97 ± 0.79	62.5 ± 15.0	24%	2.86 ± 1.21	107.5 ± 52.2	49%
Anemometer	3.29 ± 0.58	73.1 ± 27.5	38%	2.51 ± 1.05	99.6 ± 53.9	54%
HRRR	2.29 ± 0.27	50.7 ± 17.6	35%	1.81 ± 0.25	70.2 ± 25.7	37%

Uncertainty ranges reflect the combined uncertainties associated with the IME/r calculation and wind measurements (see Eq. (3)). Wind uncertainty calculations are described in Section 2.2 for HRRR, Section 3.2 for TODWL, and Section 5.1.2. for anemometer.
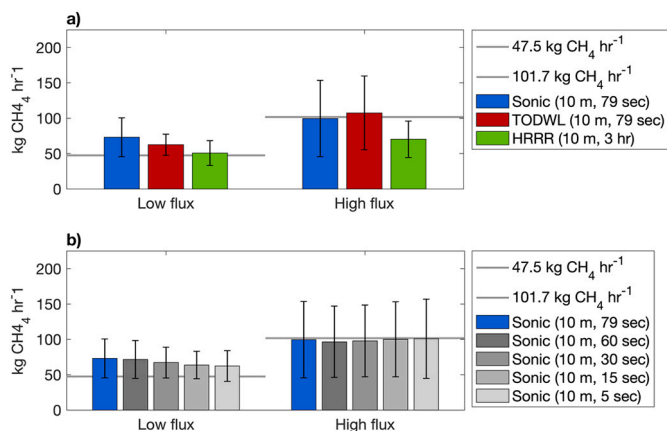

Fig. 9. a) AVIRIS-NG CH$_4$ emission rates estimated using ultrasonic anemometer (sonic), TODWL, and HRRR reanalysis data for controlled emission rate of 47.5 kg CH$_4$ hr^{-1} (before 20.2 UTC) and 101.7 kg CH$_4$ hr^{-1} (after 20.2 UTC) as shown by horizontal grey lines. Boxes denote average values and error bars indicate standard deviation. b) Emission rates derived using reduced time windows for averaging ultrasonic anemometer (sonic) observations, showing modest improvement in accuracy for the low flux example.

TODWL (red), and HRRR results (green). During the period of the low release rate, the HRRR mean flux (50.7 ± 17.6 kg CH$_4$ hr^{-1}) was very close to the actual rate, while anemometer and TODWL were high by 54% and 32%, respectively (Table 1). In contrast, during the high release rate period when observed winds varied considerably, both anemometer and TODWL mean fluxes were within 6% of the known rate. The HRRR results were significantly underestimated (70.2 ± 25.7 kg CH$_4$ hr^{-1}, 30% lower) and consistent with the tendency for HRRR winds to be too slow (Fig. 5a). This is also consistent with a previous study that reported HRRR wind estimates were 50% lower on average than the National Weather Service 5 min observations (Duren et al., 2019). As shown in Table 1, the average emission rate uncertainty ranged from 24 to 49% for TOWDL, 38–54% for the anemometer, and 35–37% for HRRR. The TODWL emission rate uncertainties are similar to the 30% mean uncertainty reported in a previous study using HRRR winds only (Duren et al., 2019).

Given the variable wind speeds during the entire controlled release experiment (Fig. 5a), the interval over which anemometer measurements were averaged was adjusted to assess the effect on the average emission rates. The resulting average emission rates are plotted in Fig. 9b using the original 79 s interval as well as 60, 30, 15, and 5 s. For the low flux example, reductions in the interval resulted in modest improvements, however, results remained similar for the high flux example. Given differences between AVIRIS-NG and TODWL observation times (Section 3.2), additional results obtained using AVIRIS-NG observation times are provided in Appendix C.

5.2. Energy, waste management, and dairy sector examples

For the San Francisco Bay Area refinery, landfill, wastewater facility, and San Joaquin Valley dairy digester, CH$_4$ plumes were visible and

consistent with TODWL wind measurements. Overall, these examples demonstrate dynamic wind conditions, the impact of local terrain on surface winds, and the ability of TODWL to accurately capture wind conditions consistent with both the AVIRIS-NG plume shapes as well as nearby meteorological stations. Details for these cases, including maps of wind fields, can be found in Appendix D.

Table 2 summarizes the mean emission rate estimates for each location. At the refinery, emission rate estimates were very similar using winds from HRRR and a nearby meteorological tower. TODWL winds for this case provided estimates that were approximately 20% lower. At the landfill and wastewater plants, which were located within 3 km of each other, the TODWL estimate was again lower than HRRR by 22%. The dairy case featured the lowest emission rates and here TODWL was almost 50% higher than HRRR. In this instance, TODWL wind speeds were higher than HRRR but were similar to winds measured at the surrounding meteorological stations, the closest of which was 10 km. It is also worth noting that at the dairy, the size of the plumes varied considerably between flight passes. This suggests a variable emission rate of the source, underlying the need for multiple observations to constrain estimates.

6. Discussion and conclusion

Accurate wind speeds are critical to estimating emissions and previous studies indicate that considerable uncertainties in wind speed propagate into emission rates (Varon et al., 2018, 2019; Jongaramrungruang et al., 2019; Duren et al., 2019). HRRR wind speeds have limited temporal and spatial resolution, meteorological station wind data are of variable quality and are often not available near observed plumes, and the use of anemometers is impractical for AVIRIS-NG flight campaigns with daily coverage of thousands of square kilometers. Given these limitations, this study focused on the use of TODWL to measure near surface winds and provide coincident measurements to CH$_4$ plumes observed with AVIRIS-NG.

The controlled release experiment provided the best opportunity to evaluate TODWL wind measurements against in situ anemometer readings and HRRR modelled winds. During the experiment, conditions were challenging given highly variable wind speeds (0–8 m s^{-1}) and directions (0–360°) along with extreme flight level instability. Despite this, TODWL measurements generally agreed well with the anemometer data (Fig. 5), with both yielding a mean wind speed of 2.9 m s^{-1} averaged over the flight period. Wind directions inferred from AVIRIS-NG

Table 2

Estimated mean CH$_4$ emissions (kg CH$_4$ hr^{-1}) from HRRR and TODWL for four CH$_4$ sources.

Source	Refinery	Landfill	Wastewater Plant	Dairy
HRRR	445.6 ± 134.4	3198.9 ± 1297.6	836.3 ± 293.2	132.5 ± 22.2
TODWL	353.7 ± 129.7	2418.7 ± 910.4	671.3 ± 235.3	196.3 ± 47.0
BAAQMD tower	446.2 ± 121.8			

Percentage differences mentioned in text are relative to HRRR values.

plume shapes were consistent with the anemometer, but in some cases did not agree with the TODWL measurements. Differences between TODWL and anemometer wind measurements and AVIRIS-NG plume shapes could largely be explained by (1) the spatial (16 km^2) and temporal averaging inherent in the TODWL measurements and (2) instrument limitations that prevented measurements below 30 m AGL. The inability to obtain TODWL winds below 30 m and the unknown height of the methane plume were two of the most significant limitations of the present study. This was especially evident during the second half of the experiment when there were significant differences at times in the 10 m wind directions from anemometer and those observed by TODWL at 30 m. The presence of small scale rapidly shifting wind conditions was also evidenced by cyclonic curvature and plume rotations in the AVIRIS-NG imagery (Figs. 4 and 6).

Emission rates and uncertainties were estimated using HRRR, anemometer, and TODWL wind speeds for each flight pass (Fig. 8) and average emission rates were calculated for the 47.5 and 101.7 kg CH$_4$ hr^{-1} flux periods (Fig. 9a and Table 1). Overall, there was better agreement between flight passes for the metered rate of 47.5 kg CH$_4$ hr^{-1} before 20.0 UTC when wind conditions were stable and closer to steady state, resulting in plumes that typically appeared more linear. During the low flux period, both anemometer and TODWL over-estimated emissions but the known emission rate falls within the error bars for each (Fig. 9a). After 20.0 UTC, wind speeds and directions became highly variable, resulting in plumes that often appeared less linear with eddies and plume rotations (Figs. 4, 6). This led to greater disagreement between flight passes for the metered rate of 101.7 kg CH$_4$ hr^{-1}. Despite the increased pass-to-pass variability during the high flux period, mean TODWL and anemometer flux estimates were very close (within 6%) to the true rate while HRRR results tended to be significantly lower (with the known rate outside of the error bars). The higher emission rate typically led to longer plumes (99 m average) compared to the low emission rate (49 m average). For the higher emission rate, the longer plumes could have downwind portions rising to a greater height, which could explain why the TODWL and anemometer 10 m wind speeds resulted in improved estimates. In contrast, during the low rate period plumes might remain closer to the ground, in which case the 10 m winds could over-estimate emission rates.

Significant outliers were present during both periods (Fig. 8); for example, the anemometer flux estimate at 19.8 UTC and the TODWL estimate at 20.9 UTC over-estimated the known release rate by 156% and 98%, respectively. In contrast, at 20.3 UTC all the emission estimates were low, especially that based on the anemometer which was 83% below the true metered rate. Overall, there were larger pass-to-pass fluctuations in emission estimates during the high rate period when winds were more variable. Calculated flux rate uncertainties increased from 24% to 49% using anemometer winds, and from 38% to 54% using TODWL winds. Despite the fluctuations, the mean flux estimates over the 7 high rate passes, from both TODWL and anemometer, were very close to the metered rate. This indicates the need for multiple observations to capture the emission variability and reduce the uncertainty of the average emission profile rather than relying on a single observation that can be highly uncertain, especially when wind fields are complex and variable.

Beyond the controlled release experiment, CH$_4$ plumes were visible and indicated wind conditions consistent with TODWL wind measurements at a San Francisco Bay Area refinery, landfill, wastewater facility, and San Joaquin Valley dairy digester. Furthermore, TODWL winds tended to agree well with meteorological station data for these examples. It is worth noting that in some cases, the closest meteorological station was around 10 km from the observed CH$_4$ plume. At times, TODWL revealed large-scale homogeneous wind fields (mainly at the dairy and landfill/wastewater sites) and in these cases, use of a distant meteorological station might be justified. However, at the controlled release site and the refinery (the latter featuring complex coastal terrain), small scale or rapidly changing wind fields were identified.

These cases underscore the potential benefits of using TODWL wind measurements to improve emission estimates. Given the temporal shortcomings of modelled wind datasets like HRRR and the sparsity of meteorological stations, the ability to measure near surface winds directly using an airborne Doppler wind lidar offers the potential to improve emission estimates of CH$_4$ point sources observed with AVIRIS-NG.

In this study, AVIRIS-NG and TODWL were hosted on different aircraft, resulting in measurements that were not acquired at exactly the same time. For example, the average time difference between AVIRIS-NG and TODWL measurements for the controlled release experiment was 49.4 s. Furthermore, TODWL wind retrievals were typically closer to 30 m above the ground, requiring a power law adjustment to permit direct comparisons with 10 m anemometer wind measurements. Future studies could incorporate additional anemometer measurements at multiple locations and heights above ground, ideally as high as 30 m, to better define near-surface winds and permit direct comparison to TODWL wind retrievals. In addition, the use of a broader range of controlled release emission rates would permit a better assessment of the accuracy of estimated emission rates. Finally, given the controlled release experiment occurred under challenging conditions characterized by strong heating and turbulence, future experiments should explore performance under different conditions, including different times of day and during periods characterized by less variable wind. Ideally, additional studies would also be performed in an environment with higher wind speeds (5–10 m s^{-1}) which would enable more statistically significant comparisons between the ground-based and airborne wind speeds and flux estimates.

Over the 15 years since TODWL was built there have been significant advances in Doppler wind lidar technology including reductions in size, weight, and power. Currently available state of the art Doppler wind lidars can retrieve winds below 30 m AGL using a nadir viewing geometry for an aircraft flying at altitudes greater than 500 m (e.g. 3–10 km). Therefore, an airborne wind lidar system and imaging spectrometer could be co-manifested on one aircraft flying well above the turbulent boundary layer to provide wind measurements with improved spatial and temporal overlap with observed CH$_4$ plumes. This would likely lower the operational costs to utilize an imaging spectrometer in conjunction with a wind lidar system and further reduce uncertainty of the CH$_4$ emission estimates by ensuring concurrent measurements. In addition, an airborne Doppler wind lidar can be used to map complex wind fields and identify conditions when emission estimates are likely to be more uncertain in real time. When complex or variable wind fields are identified, additional flight passes could be acquired to help reduce emission rate uncertainty at a given site. This could be particularly important for plumes from different emission sectors that are often highly intermittent (Duren et al., 2019) or have highly variable plume shapes and emission rates (Figs. 4, 6) as well as sites located in complex terrain or near coastlines where highly variable wind fields could be expected.

Declaration of Competing Interest

The authors declare that they have no known competing financial interests or personal relationships that could have appeared to influence the work reported in this paper.

Acknowledgments

Appendix A. HRRR winds

U10 (zonal wind speed 10 m above ground) and V10 (meridional wind speed 10 m above ground) meteorological fields in the High Resolution Rapid Refresh (HRRR; Dowell, 2020) model of the National Oceanic and Atmospheric Administration (NOAA) were used to compute wind speed at plume location. Windspeed from U10 and V10 meteorological fields can be computed as:

$$WS = \sqrt{U10^2 + V10^2} \tag{5}$$

where WS stands for windspeed. As U10 and V10 meteorological fields do not provide uncertainty estimates, variability in these fields was used to represent uncertainty. Mean and standard deviation (SD) of windspeed was calculated by using the 9 nearest grid cells to the plume location for the nearest hour and $\pm$ 1 h.

Appendix B. Comparison of wind measurements and flux estimates

Direct comparison of individual wind measurements from the anemometer, TODWL, and HRRR is complicated by the differences in how these winds are derived and what they represent. The anemometer is a continuous point measurement while each TODWL wind vector represents an average or integration of individual line of sight velocity measurements obtained within a 16 km^2 (and 20 m deep) box. Under extremely specific conditions, such as a very homogeneous wind field, the two measurements should be very similar. However, when there is wind variability within the sampled region, an individual TODWL wind speed should not be expected to replicate an anemometer wind speed.

That said, over multiple passes, the differences should largely average out unless there is a persistent wind anomaly somewhere in the sampled region. This was observed over the 14 controlled release passes, where the anemometer and TODWL yielded the same mean wind speed (2.9 m s^{-1}). For the low and high emission rate period there were some differences in the means - during the low rate the mean wind speeds were 3.29 m s^{-1} for anemometer and 2.97 m s^{-1} for TODWL, while for the high rate period the means were 2.51 m s^{-1} for anemometer and 2.86 m s^{-1} for TODWL. These differences are still fairly small, on the order of 10–15%.

With these caveats in mind, in this section additional comparisons between individual wind measurements from the various sources are presented. Fig. B1 compares TODWL wind speeds to wind speeds measured from the anemometer and meteorological stations. Panel a shows the 14 cases from the controlled release flights while panel b adds additional comparisons from the other study sites that were flown (these were comparisons between TODWL and the nearest meteorological station). The plots reveal a fair amount of scatter but no evidence of an overall bias – the data points are roughly evenly distributed around the y = x line. Furthermore, as discussed previously, the mean wind speeds from the TODWL and the anemometer are the same over the 2.5 h controlled release experiment. Two linear fits are included on the plots - standard ordinary least squares (OLS, dashed) and model 2 (thick solid) least squares which minimizes the orthogonal distances to each data point. The OLS fits suggest a significant deviation from y = x (slopes from 0.32 to 0.42) while the model 2 fits have slopes closer to 1 (0.79 and 1.22). RMSE values from both fits are similar. These fits should be viewed with caution due to the low number of data points (14 and 29) and the limited range of wind speeds sampled during the flights. However, it is worth noting that the inclusion of the additional meteorological stations in panel b does slightly improve the quality of the fit, which suggests additional measurements over a wider range of wind speeds should lead to further improvements and increased confidence in the applicability of TODWL winds.
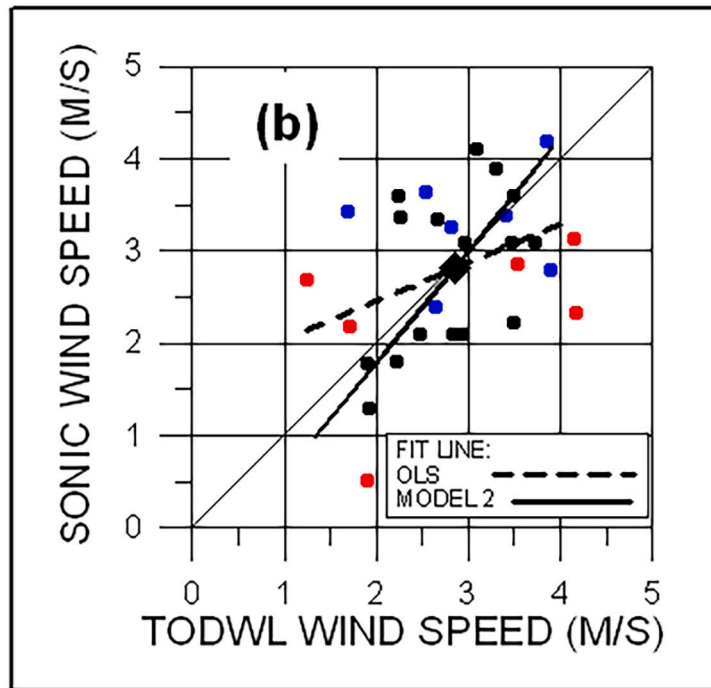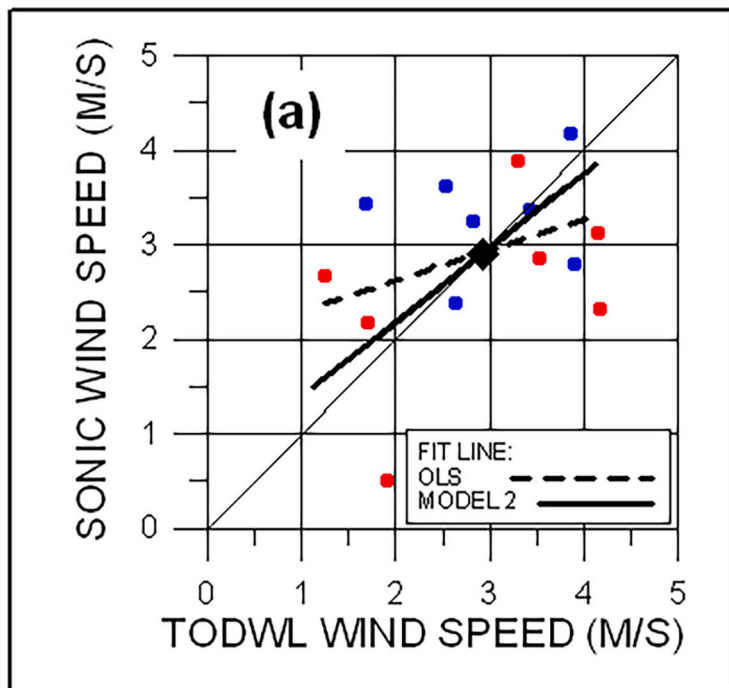
Fig. B1. Comparison of wind speed measurements from TODWL, the anemometer, and meteorological stations. a) TODWL wind speed versus ultrasonic anemometer (sonic) wind speed for the 14 controlled release cases. Blue markers indicate data from low emission rate period; red markers indicate data from high rate period. Large diamond marks dataset mean. Ordinary least squares fit (OLS; $y = 0.32\times + 1.97$, RMSE $= 0.85$ m s^{-1}) shown as heavy dashed line; model 2 fit ($y = 0.79\times + 0.59$, RMSE $= 0.79$ m s^{-1}) shown as thick solid line. Thin black line represents $y = x$. b) As in a but with data from the non-controlled release cases (meteorological stations, black circles) included. Ordinary least squares fit: $y = 0.42\times + 1.62$, RMSE $= 0.81$ m s^{-1}; model 2 fit: $y = 1.22\times -0.65$, RMSE $= 0.66$ m s^{-1}. (For interpretation of the references to colour in this figure legend, the reader is referred to the web version of this article.)

Fig. B2 shows scatter plots for HRRR wind speed versus (a) the anemometer and (b) TODWL for the controlled release case. The HRRR winds are obviously clustered indicating a significant low bias against both anemometer and TODWL. Comparison to Fig. B1 shows that for this sample, the TODWL and anemometer winds are more consistent with each other while HRRR winds show little relation to either anemometer or TODWL. This supports the conclusion that targeted TODWL winds should provide improved wind speed estimates compared to HRRR. However, our ability to draw statistically significant conclusions is limited by the extremely small range of winds speeds available from the HRRR in these cases.
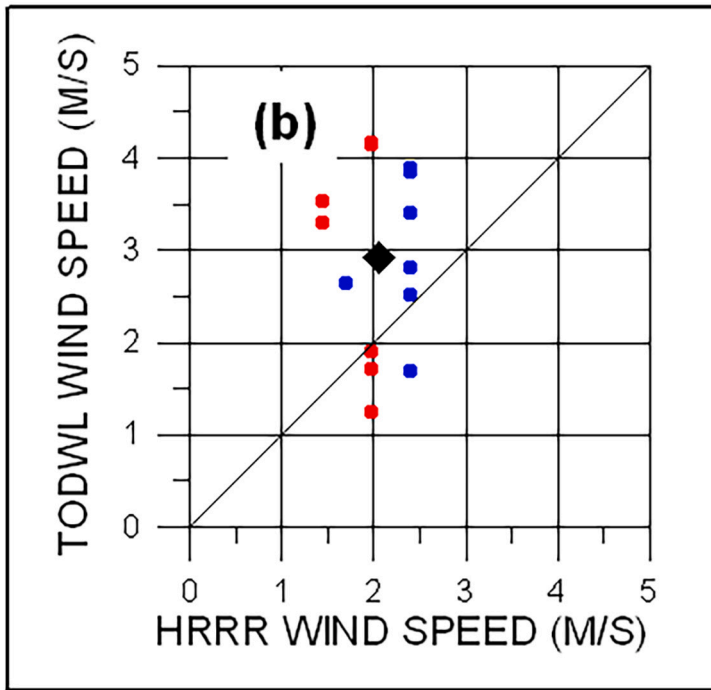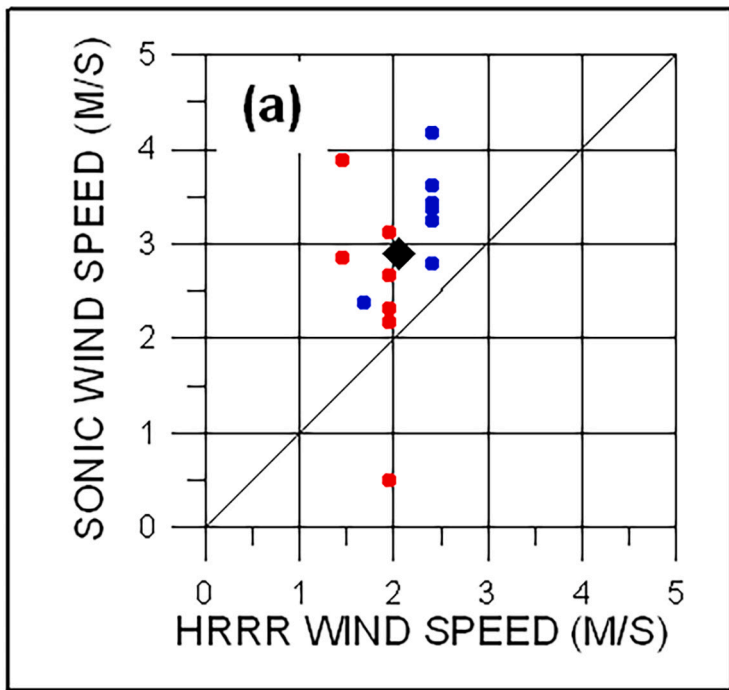

Fig. B2. Comparison of wind speeds for the controlled release case. a) HRRR versus ultrasonic anemometer (sonic) b) HRRR versus TODWL. Blue markers indicate data from low emission rate period; red markers indicate data from high rate period. Large diamond marks dataset mean. Thin solid line represents $y = x$. (For interpretation of the references to colour in this figure legend, the reader is referred to the web version of this article.)

Fig. B3 shows scatterplots for emission rate estimates for TODWL versus anemometer and TODWL vs HRRR for the controlled release case. Once again, despite the scatter, there is little evidence of bias in the TODWL/anemometer flux estimates. In comparison, the HRRR flux estimates are strongly low-biased. Interestingly, the fit lines in panel a suggests a better relationship between anemometer and TODWL flux estimates than what was found for the wind speeds alone. Again, though, it is difficult to draw substantive conclusions given that only two release rates were sampled.
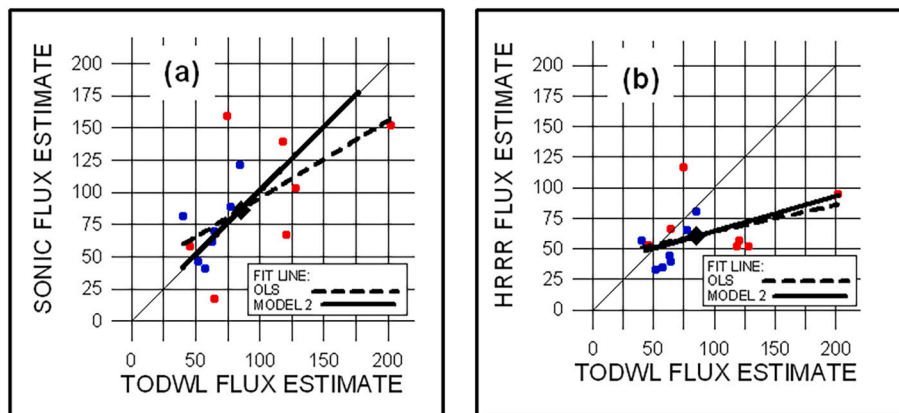

Fig. B3. Scatterplots of TODWL flux estimates versus a) ultrasonic anemometer (sonic) and b) HRRR for the controlled release case. Blue markers indicate data from low emission rate period; red markers indicate data from high rate period. Large diamond marks dataset mean. Fit lines as in Fig. B1. For panel a, ordinary least squares fit $y = 0.60\times + 35.2$ with RMSE = 35.9, model 2 fit $y = 0.99\times + 2.26$ with RMSE = 28.5. For panel b, ordinary least squares fit $y = 0.22\times + 41.9$ with RMSE = 22.3, model 2 fit $y = 0.28\times + 36.4$ with RMSE = 21.6 Flux units: kg CH_4 hr^{-1}. (For interpretation of the references to colour in this figure legend, the reader is referred to the web version of this article.)

Overall, the ability to determine correlations/fits between various wind and flux estimates is limited by the relatively low number of observations as well as the limited range of measured wind speeds. Most measurements from the anemometer and TODWL fell between 1.5 and 4.5 m s^{-1} while HRRR wind speeds were even more limited in range. In order to demonstrate a statistically significant relationship, additional measurements over a wider range of wind speeds (as well as emission rates) would be required.

Appendix C. Emission estimates using times derived from AVIRIS-NG plumes

Differences between AVIRIS-NG and TODWL observation times were discussed in Section 3.2. Below, emission estimates are presented using the AVIRIS-NG observation times. These results appear similar to those obtained using TODWL observation times (see Figs. 8, 9 in Section 5.1.3).
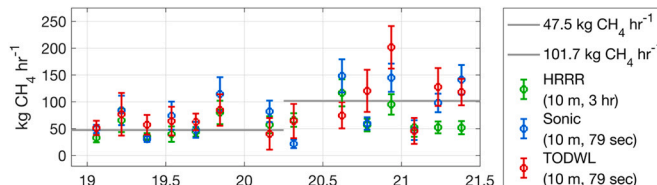

Fig. C1. AVIRIS-NG CH_4 emission rates derived using TODWL, ultrasonic anemometer (sonic), and HRRR reanalysis wind data for AVIRIS-NG observation times. Two known controlled release emission rates are plotted as horizontal grey lines for 47.5 and 101.7 kg CH_4 hr^{-1}.
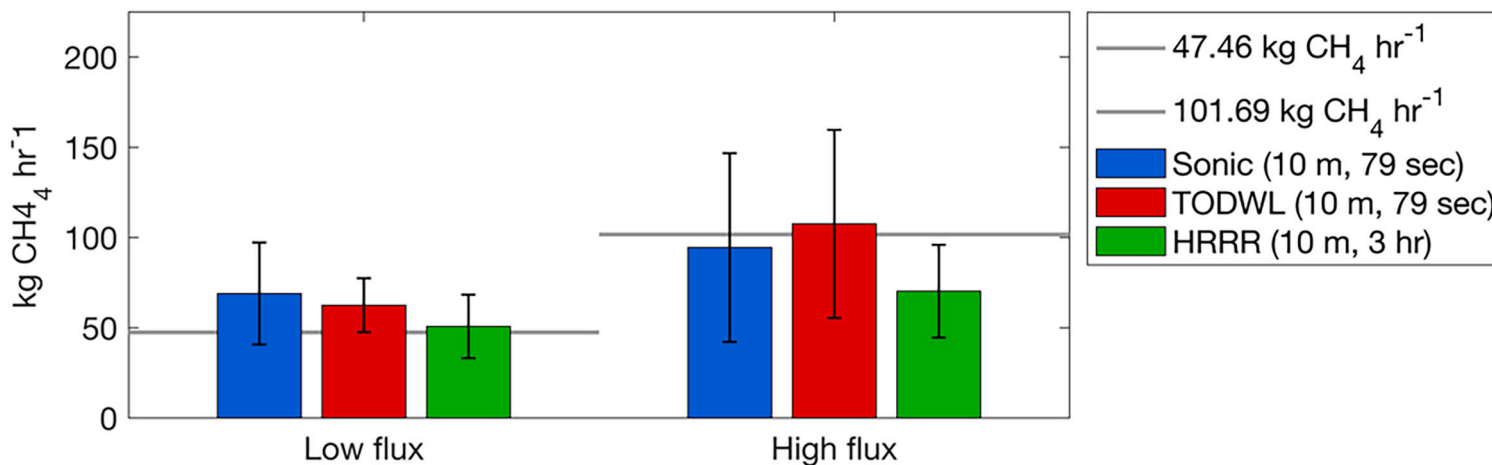

Fig. C2. AVIRIS-NG CH_4 emission rates estimated using ultrasonic anemometer (sonic), TODWL, and HRRR reanalysis data for AVIRIS-NG observation times. Controlled emission rate of 47.5 kg CH_4 hr^{-1} (before 20.2 UTC) and 101.7 kg CH_4 hr^{-1} (after 20.2 UTC) as shown by horizontal grey lines). Boxes denote average values and error bars indicate standard deviation.

Appendix D. Refinery, landfill, wastewater facility, and dairy digester examples

Fig. D1 shows the second pass at the refinery on 20 Sept. with an observed CH_4 plume originating from a hydrogen plant (Guha et al., 2020). Wind speeds from HRRR and the BAAQMD tower were nearly identical at 3.3 to 3.4 m s^{-1}. The TODWL wind during pass 2 was similar (3.4 m s^{-1}) but was much lower during pass 1 (1.5 m s^{-1}). As a result, while mean emission rate estimates from HRRR and BAAQMD were nearly identical, TODWL was about 20% lower (Table 2). TODWL wind directions were generally consistent with nearby stations and captured both the SSE winds over water west of the refinery and the turn to SW over land. The one area of disagreement was at Richmond (point c), which reported winds from the SE while TODWL was showing SW. This could reflect a shallow/localized terrain-based flow that was not resolvable by TODWL. The AVIRIS-NG plumes showed SSW winds with variations in plume shape and direction similar to those seen in the controlled release case. This indicates the dynamic nature of these emissions and the impact of variable wind conditions on plume appearance.
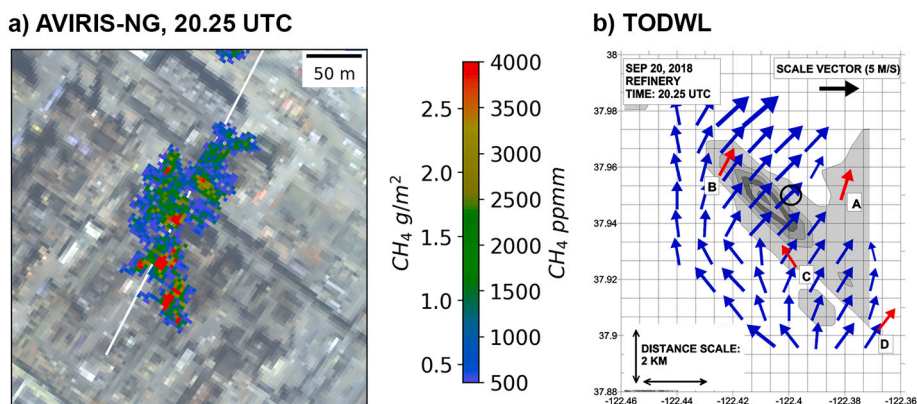

a) AVIRIS-NG, 20.25 UTC

b) TODWL

Fig. D1. a) AVIRIS-NG CH_4 plume overlaid on true colour imagery for a San Francisco Bay area refinery for 20.3 UTC 20 Sept. 2018. White line indicates estimated wind direction (207°) derived from plume shape. b) TODWL near surface wind field for the same time. Wind vectors for TODWL (blue) and meteorological stations (red). Grey contours show terrain every 20 m; white areas indicate water. Black circle marks refinery site. Meteorological station locations indicated for BAAQMD 2 m tower (A), San Pablo (B), Richmond (C), and Point Potrero (D). (For interpretation of the references to colour in this figure legend, the reader is referred to the web version of this article.)

Both plumes shown in Fig. D2 for 27 Sept. 2018 indicate a consistent westerly wind direction (275–279°) at the San Francisco Bay Area landfill and wastewater facility sites, which are located only 3 km apart. TODWL showed relatively homogeneous WNW flow (290–308°) across the entire region with speeds ranging between 2.5 and 3.5 m s^{-1}, somewhat lighter than HRRR (3.4–4.5 m s^{-1}). There were no meteorological stations in the analysis domain; the closest station was San Jose International Airport 8 km to the southeast which reported NW winds (320–330°) at 3.1–3.6 m s^{-1}. At Mountain View, the winds were more northerly (350°) and a little stronger (3.6–4.1 m s^{-1}). Fremont winds were more westerly and weaker, but this site was higher (180 m compared to an average 6 m elevation for the landfill and wastewater facility) and likely not representative of the conditions around the emission sites. The resulting emission rate estimates from HRRR and TODWL were within 20–25% of each other with TODWL being lower (Table 2).
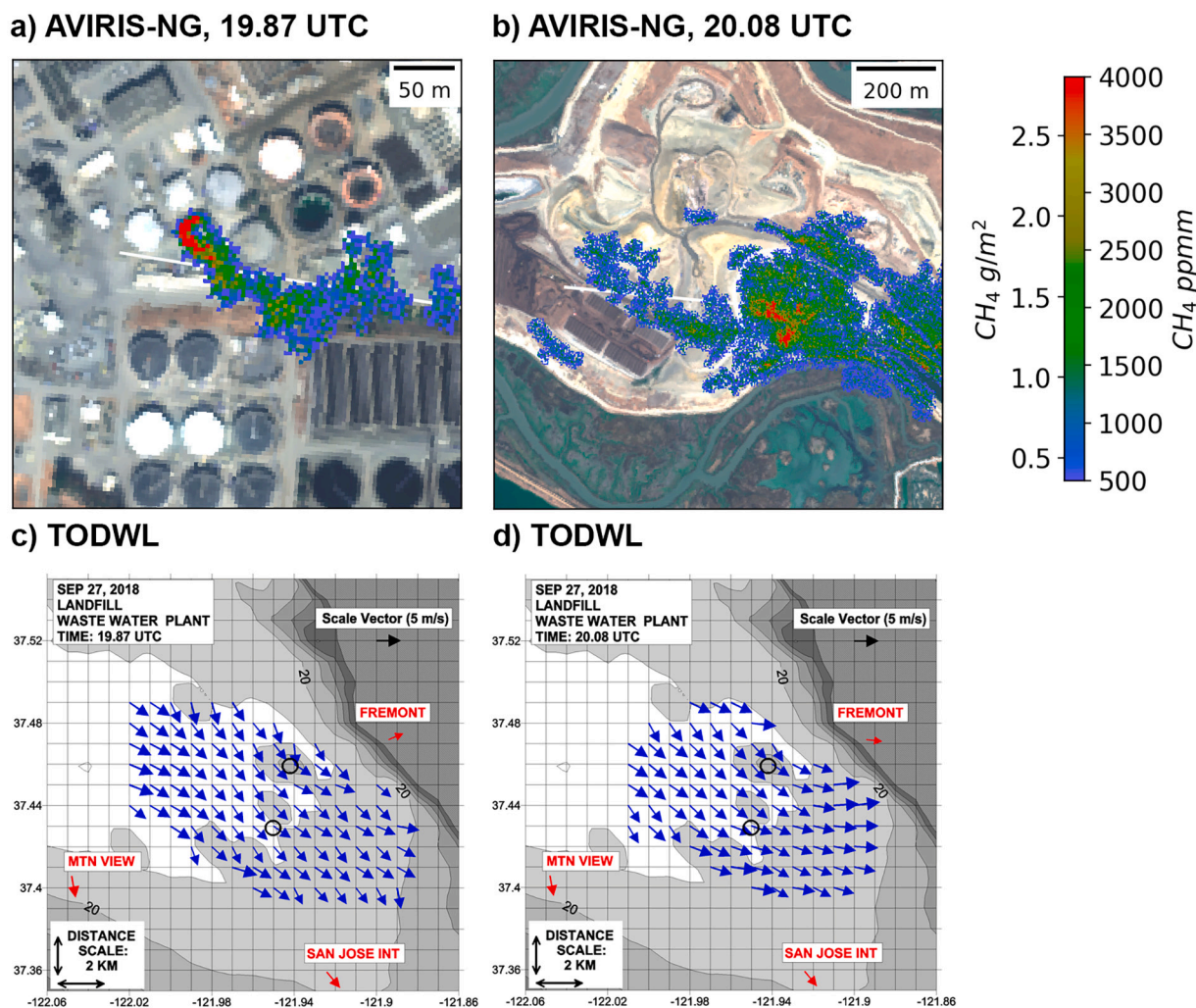
a) AVIRIS-NG, 19.87 UTC　　　b) AVIRIS-NG, 20.08 UTC

c) TODWL　　　　　　　　　d) TODWL

Fig. D2. a) AVIRIS-NG CH_4 plume overlaid on true colour imagery for 27 Sept. 2018 at San Francisco Bay Area wastewater treatment facility. White line indicates estimated wind direction derived from plume shape (279°). b) Same as panel a except for landfill plume. Inferred wind direction (276°) is consistent with winds measured from TODWL and meteorological stations. c, d) TODWL near surface wind fields associated with each plume example. Wind vectors for TODWL (blue) and meteorological stations (red). Grey contours show terrain every 20 m with white areas indicating water. Black circles indicate location of landfill (northeastern site) and wastewater treatment plant. (For interpretation of the references to colour in this figure legend, the reader is referred to the web version of this article.)

There were three observations on 19 Sept. 2018 for the dairy digester and one example is shown in Fig. D3. TODWL indicated NNW flow across the region which was consistent with the observed plumes and measurements from the nearest meteorological station (Corcoran at 10 km distance).
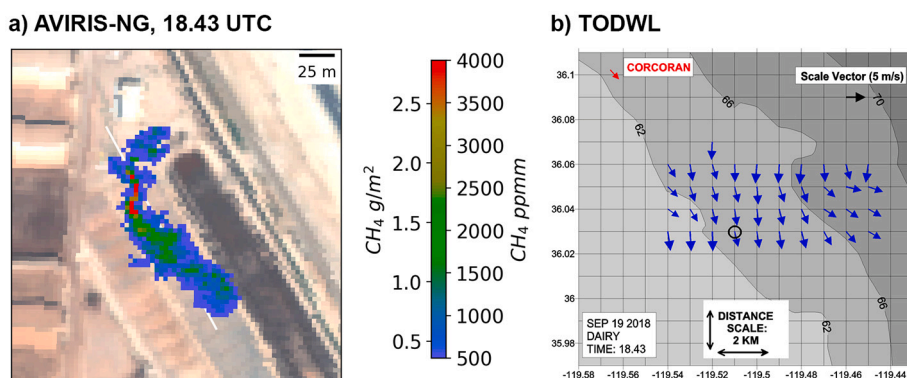
a) AVIRIS-NG, 18.43 UTC　　　b) TODWL

Fig. D3. a) AVIRIS-NG CH_4 plume overlaid on true colour imagery for dairy waste digester near Corcoran, CA at 18.4 UTC on 19 Sept. 2018. White lines indicating estimated wind direction (331°) derived from plume shape consistent with winds measured from TODWL and meteorological stations. b) TODWL wind vector field for the same time. TODWL vectors in blue, meteorological station in red. Grey contours show terrain every 4 m. Circle indicates location of dairy. (For interpretation of the references to colour in this figure legend, the reader is referred to the web version of this article.)

For this case, TODWL showed 347° versus 331° from the AVIRIS-NG plume, while at 18.8 UTC (not shown) winds direction was 332.5° from TODWL and 328.9° as inferred from the plume. TODWL wind speeds during the 3 passes ranged from 2.6 to 3.6 m s^{-1}, which were stronger than the HRRR winds (2.2 m s^{-1}) but in line with surrounding meteorological stations which ranged from 1.3 to 4.2 m s^{-1}. This case featured the lowest mean

emission rates as well as the largest difference between TODWL and HRRR (46%). It is worth noting the size of the plumes are considerably different between flight passes (not shown). This suggests a variable emission rate of the source, underlying the need for multiple observations to constrain estimates.

References

Benjamin, S.G., Weygandt, S.S., Brown, J.M., Hu, M., Alexander, C.R., Smirnova, T.G., Olson, J.B., James, E.P., Dowell, D.C., Grell, G.A., Lin, H., 2016. A north American hourly assimilation and model forecast cycle: the rapid refresh. Mon. Weather Rev. 144 (4), 1669–1694.

Brandt, A.R., Heath, G.A., Kort, E.A., O'Sullivan, F., Pétron, G., Jordaan, S.M., Tans, P., Wilcox, J., Gopstein, A.M., Arent, D., Wofsy, S., 2014. Methane leaks from north American natural gas systems. Science 343 (6172), 733–735.

Brandt, A.R., Heath, G.A., Cooley, D., 2016. Methane leaks from natural gas systems follow extreme distributions. Environ. Sci. Technol. 50 (22), 12512–12520.

Cusworth, D.H., Jacob, D.J., Varon, D.J., Chan Miller, C., Liu, X., Chance, K., Thorpe, A. K., Duren, R.M., Miller, C.E., Thompson, D.R., Frankenberg, C., 2019. Potential of next-generation imaging spectrometers to detect and quantify methane point sources from space. Atmos. Measur. Tech. 12 (10).

Cusworth, D.H., Duren, R.M., Thorpe, A.K., Tseng, E., Thompson, D., Guha, A., Newman, S., Foster, K.T., Miller, C.E., 2020. Using remote sensing to detect, validate, and quantify methane emissions from California solid waste operations. Environ. Res. Lett. 15 (5) (p.054012).

Cusworth, D.H., Duren, R.M., Thorpe, A.K., Olson-Duvall, W., Heckler, J., Chapman, J. W., Eastwood, M.L., Helmlinger, M.C., Green, R.O., Asner, G.P., Dennison, P.E., 2021. Intermittency of Large Methane Emitters in the Permian Basin. Environ. Sci. Technol. Lett. 8 (7), 567–573.

De Wekker, S.F.J., Godwin, K.S., Emmitt, G.D., Greco, S., 2012. Airborne Doppler lidar measurements of valley flows in complex coastal terrain. J. Appl. Meteorol. Climatol. 51 (8), 1558–1574.

Dowell, D., 2020. HRRR Data-Assimilation System (HRRRDAS) and HRRRE Forecasts. Available from. https://rapidrefresh.noaa.gov/internal/pdfs/2020_Spring_Experiment_HRRRE_Documentation.pdf.

Duren, R.M., Thorpe, A.K., Foster, K.T., Rafiq, T., Hopkins, F.M., Yadav, V., Bue, B.D., Thompson, D.R., Conley, S., Colombi, N.K., Frankenberg, C., 2019. California's methane super-emitters. Nature 575 (7781), 180–184.

Elder, C.D., Thompson, D.R., Thorpe, A.K., Hanke, P., Walter Anthony, K.M., Miller, C.E., 2020. Airborne mapping reveals emergent power law of arctic methane emissions. Geophys. Res. Lett. 47 (3) (p.e2019GL085707).

Emmitt, G.D., 2007. Airborne wind lidar for atmospheric boundary layer research (invited paper). In: Lidar Remote Sensing for Environmental Monitoring VIII, SPIE Optics + Photonics, San Diego, CA, 28–30 August.

Emmitt, G.D., 2019. Advanced processing of Airborne Doppler Wind Lidar wind measurements to resolve PBL circulations and near surface wind fields over the open ocean. In: AGU 100th Fall Meeting, A41L – Boundary Layer Clouds and Turbulence and Their Interaction with the Underlying Land or Ocean Surface Poster Session, San Francisco, CA, Dec. 12.

Emmitt, G.D., Greco, S., 2013. Study of airborne DWL in support of precision airdrops. In: Working Group Meeting on Space-based Lidar Winds at College Park, MD, April 17-19.

Emmitt, G.D., O'Handley, C., 2003. Airborne wind lidar to evaluate air/ocean exchanges at high wind speeds. In: Amer. Meteor. Soc. 83th Ann. Meeting, 12th Symposium on Meteorological Observations and Instrumentation (SMOI), Long Beach, CA, February.

Emmitt, G.D., O'Handley, C., 2015. Advances in C-17 wing tip vortex investigations using the TODWL. In: Working Group Meeting on Space-based Lidar Winds at Boulder, CO, Apr 27-29.

Emmitt, G.D., O'Handley, C., Greco, S., Foster, R., Brown, R., 2005a. Airborne Doppler wind Lidar investigations of OLEs over the eastern Pacific and the implications for flux parameterizations. In: Amer. Meteor. Soc. 85th Ann. Meeting, Sixth Conference on Coastal Atmospheric and Oceanic Prediction and Processes, San Diego, CA, January.

Emmitt, G.D., O'Handley, C., Wood, S.A., Greco, S., Bluth, R., Jonsson, H., 2005b. TODWL: an airborne Doppler wind lidar for atmospheric research. In: Amer. Meteor. Soc. 85th Ann. Meeting, 2nd Symposium on Lidar Atmospheric Applications, San Diego, CA, January.

Emmitt, G.D., Godwin, K.S., Greco, S., O'Handley, C., 2014a. Advanced airborne Doppler Wind Lidar signal processing for observations in complex terrain (Invited Paper). In: SPIE Remote Sensing at Amsterdam, NL. Conference 9246: Lidar Technologies, Techniques, and Measurements for Atmospheric Remote Sensing [9246-8], Sep 22-15.

Emmitt, G.D., O'Handley, C., Godwin, K., 2014b. Airborne DWL investigations of wing tip vortices and their dissipation. In: Working Group Meeting on Space-based Lidar Winds at Boulder CO, May 13-14.

Emmitt, G.D., Foster, R.C., De Wekker, S.F.J., Godwin, K.S., 2015a. Airborne Doppler Wind Lidar investigations of OLEs and LLJs in the marine boundary layer and their implications for flux parameterization. In: Amer. Meteor. Soc. 95th Ann. Meeting, Session: Coastal and marine boundary layers in the atmosphere and ocean. January 04–08, 2015, Phoenix Az.

Emmitt, G.D., Greco, S., Godwin, K., 2015b. Using TODWL soundings to establish expectations for precision airdrops. In: Working Group Meeting on Space-based Lidar Winds at Miami FL, Nov 2-4.

Emmitt, G.D., Wood, S.A., Greco, S., O'Handley, C., 2017. Atmospheric energy harvesting for autonomous in-flight path planning of a UAV instrumented with Doppler wind Lidar. In: Working Group on Space-based Lidar Winds, Hampton, Va, March 21-13.

Foote, M.D., Dennison, P.E., Thorpe, A.K., Thompson, D.R., Jongaramrungruang, S., Frankenberg, C., Joshi, S.C., 2020. Fast and accurate retrieval of methane concentration from imaging spectrometer data using sparsity prior. IEEE Trans. Geosci. Remote Sens. 58 (9), 6480–6492.

Frankenberg, C., Thorpe, A.K., Thompson, D.R., Hulley, G., Kort, E.A., Vance, N., Borchardt, J., Krings, T., Gerilowski, K., Sweeney, C., Conley, S., 2016. Airborne methane remote measurements reveal heavy-tail flux distribution in four corners region. Proc. Natl. Acad. Sci. 113 (35), 9734–9739.

Godwin, K.S., De Wekker, S.F.J., Emmitt, G.D., 2012. Retrieving winds in the surface layer over land using an airborne Doppler lidar. J. Atmos. Ocean. Technol. 29 (4), 487–499.

Greco, S., Emmitt, G.D., 2005. Investigation of flows within complex terrain and along coastlines using an airborne Doppler wind lidar: observations and model comparisons. In: Amer. Meteor. Soc. 85th Ann. Meeting, Sixth Conference on Coastal Atmospheric and Oceanic Prediction and Processes, San Diego, CA, January.

Guha, A., Newman, S., Fairley, D., Dinh, T.M., Duca, L., Conley, S., Smith, M.L., Thorpe, A., Duren, R.M., Cusworth, D., Foster, K., 2020. Assessment of regional methane emissions inventories through airborne quantification in the San Francisco Bay Area. Environ. Sci. Technol. 54 (15), 9254–9264.

Hamlin, L., Green, R.O., Mouroulis, P., Eastwood, M., Wilson, D., Dudik, M., Paine, C., 2011, March. Imaging spectrometer science measurements for terrestrial ecology: AVIRIS and new developments. In: 2011 Aerospace Conference. IEEE, pp. 1–7.

Hopkins, F.M., Ehleringer, J.R., Bush, S.E., Duren, R.M., Miller, C.E., Lai, C.T., Hsu, Y.K., Carranza, V., Randerson, J.T., 2016. Mitigation of methane emissions in cities: how new measurements and partnerships can contribute to emissions reduction strategies. Earth's Future 4 (9), 408–425.

Jongaramrungruang, S., Frankenberg, C., Matheou, G., Thorpe, A.K., Thompson, D.R., Kuai, L., Duren, R.M., 2019. Towards accurate methane point-source quantification from high-resolution 2-D plume imagery. Atmos. Measur. Tech. 12 (12).

Kirschke, S., Bousquet, P., Ciais, P., Saunois, M., Canadell, J.G., Dlugokencky, E.J., Bergamaschi, P., Bergmann, D., Blake, D.R., Bruhwiler, L., Cameron-Smith, P., 2013. Three decades of global methane sources and sinks. Nat. Geosci. 6 (10), 813–823.

Krautwurst, S., Gerilowski, K., Jonsson, H.H., Thompson, D.R., Kolyer, R.W., Iraci, L.T., Thorpe, A.K., Horstjann, M., Eastwood, M., Leifer, I., Vigil, S.A., 2017. Methane emissions from a Californian landfill, determined from airborne remote sensing and in situ measurements. Atmos. Measur. Tech. 10 (9), 3429.

Lyon, D.R., Zavala-Araiza, D., Alvarez, R.A., Harriss, R., Palacios, V., Lan, X., Talbot, R., Lavoie, T., Shepson, P., Yacovitch, T.I., Herndon, S.C., 2015. Constructing a spatially resolved methane emission inventory for the Barnett shale region. Environ. Sci. Technol. 49 (13), 8147–8157.

Myhre, G., Shindell, D., Bréon, F.-M., Collins, W., Fuglestvedt, J., Huang, J., Koch, D., Lamarque, J., Lee, D., Mendoza, B., Nakajima, T., Robock, A., Stephens, G., Takemura, T., Zhang, H., 2013. Anthropogenic and natural radiative forcing. In: Climate Change 2013: The Physical Science Basis. Contribution of Working Group I to the Fifth Assessment Report of the Intergovernmental Panel on Climate Change, Tech. Rep.

Newman, J.F., Kein, P.M., 2014. The impacts of atmospheric stability on the accuracy of wind speed extrapolation methods. Resources 3 (1), 81–105.

Nisbet, E.G., Manning, M.R., Dlugokencky, E.J., Fisher, R.E., Lowry, D., Michel, S.E., Myhre, C.L., Platt, S.M., Allen, G., Bousquet, P., Brownlow, R., 2019. Very strong atmospheric methane growth in the 4 years 2014–2017: implications for the Paris agreement. Glob. Biogeochem. Cycles 33 (3), 318–342.

Pal, S., De Wekker, S.F.J., Emmitt, G.D., 2016. Investigation of the spatial variability of the convective boundary layer heights over an isolated mountain: cases from the materhorn-2012 experiment. J. Appl. Meteorol. Climatol. 55 (9), 1927–1952.

Schaefer, H., Fletcher, S.E.M., Veidt, C., Lassey, K.R., Brailsford, G.W., Bromley, T.M., Dlugokencky, E.J., Michel, S.E., Miller, J.B., Levin, I., Lowe, D.C., 2016. A 21st-century shift from fossil-fuel to biogenic methane emissions indicated by 13CH4. Science 352 (6281), 80–84.

Schwietzke, S., Sherwood, O.A., Bruhwiler, L.M., Miller, J.B., Etiope, G., Dlugokencky, E. J., Michel, S.E., Arling, V.A., Vaughn, B.H., White, J.W., Tans, P.P., 2016. Upward revision of global fossil fuel methane emissions based on isotope database. Nature 538 (7623), 88–91.

Thompson, D.R., Leifer, I., Bovensmann, H., Eastwood, M., Fladeland, M., Frankenberg, C., Gerilowski, K., Green, R.O., Kratwurst, S., Krings, T., Luna, B., 2015. Real-time remote detection and measurement for airborne imaging spectroscopy: a case study with methane. Atmos. Meas. Tech. 8 (10), 4383–4397.

Thorpe, A.K., Frankenberg, C., Roberts, D.A., 2014. Retrieval techniques for airborne imaging of methane concentrations using high spatial and moderate spectral resolution: application to AVIRIS. Atmos. Measur. Tech. 7 (2), 491–506.

Thorpe, A.K., Frankenberg, C., Aubrey, A.D., Roberts, D.A., Nottrott, A.A., Rahn, T.A., Sauer, J.A., Dubey, M.K., Costigan, K.R., Arata, C., Steffke, A.M., 2016. Mapping methane concentrations from a controlled release experiment using the next generation airborne visible/infrared imaging spectrometer (AVIRIS-NG). Remote Sens. Environ. 179, 104–115.

Thorpe, A.K., Frankenberg, C., Thompson, D.R., Duren, R.M., Aubrey, A.D., Bue, B.D., Green, R.O., Gerilowski, K., Krings, T., Borchardt, J., Kort, E.A., 2017. Airborne DOAS retrievals of methane, carbon dioxide, and water vapor concentrations at high spatial resolution: application to AVIRIS-NG. Atmospheric Measurement Techniques 10 (10), 3833–3850.

Thorpe, A.K., Duren, R.M., Conley, S., Prasad, K.R., Bue, B.D., Yadav, V., Foster, K.T., Rafiq, T., Hopkins, F.M., Smith, M.L., Fischer, M.L., 2020. Methane emissions from underground gas storage in California. Environ. Res. Lett. *15* (4), 045005.

Varon, D.J., Jacob, D.J., McKeever, J., Jervis, D., Durak, B.O., Xia, Y., Huang, Y., 2018. Quantifying methane point sources from fine-scale satellite observations of atmospheric methane plumes. Atmos. Measur. Tech. 11 (10).

Varon, D.J., McKeever, J., Jervis, D., Maasakkers, J.D., Pandey, S., Houweling, S., Aben, I., Scarpelli, T., Jacob, D.J., 2019. Satellite discovery of anomalously large methane point sources from oil/gas production. Geophys. Res. Lett. 46 (22), 13507–13516.

Zavala-Araiza, D., Lyon, D., Alvarez, R.A., Palacios, V., Harriss, R., Lan, X., Talbot, R., Hamburg, S.P., 2015. Toward a functional definition of methane super-emitters: application to natural gas production sites. Environ. Sci. Technol. 49 (13), 8167–8174.